THE FABRIC OF CLASTS, VEINS AND FOLIATIONS WITHIN THE ACTIVELY CREEPING ZONES OF THE SAN ANDREAS FAULT AT SAFOD: IMPLICATIONS FOR DEFORMATION PROCESSES

A Thesis

by

DAVID WAYNE SILLS

Submitted to the Office of Graduate Studies of
Texas A&M University
in partial fulfillment of the requirements for the degree of

MASTER OF SCIENCE

December 2010

Major Subject: Geology

The Fabric of Clasts, Veins and Foliations within the
Actively Creeping Zones of the San Andreas Fault at SAFOD: Implications for
Deformation Processes

THE FABRIC OF CLASTS, VEINS AND FOLIATIONS WITHIN THE ACTIVELY CREEPING ZONES OF THE SAN ANDREAS FAULT AT SAFOD: IMPLICATIONS FOR DEFORMATION PROCESSES

A Thesis

by

DAVID WAYNE SILLS

Submitted to the Office of Graduate Studies of
Texas A&M University
in partial fulfillment of the requirements for the degree of

MASTER OF SCIENCE

Approved by:

Chair of Committee,	Judith Chester
Committee Members,	Frederick Chester
	David Schechter
Head of Department,	Andreas Kronenberg

December 2010

Major Subject: Geology

ABSTRACT

The Fabric of Clasts, Veins and Foliations within the
Actively Creeping Zones of the San Andreas Fault at SAFOD: Implications for
Deformation Processes. (December 2010)
David Wayne Sills, B.S., Sam Houston State University;
M.S., Texas A&M University
Chair of Advisory Committee: Dr. Judith Chester

Recovered core samples from the San Andreas Fault Observatory at Depth (SAFOD), located near Parkfield, CA, offer a unique opportunity to study the products of faulting and to learn about the mechanisms of slip at 3 km depth. Casing deformation reflects active creep along two strands of the San Andreas Fault (SAF) at SAFOD. The two fault strands are referred to as the Southwest Deforming Zone (SDZ) at 3194 m measured depth (MD) and the Central Deforming Zone (CDZ) at 3301 m MD. The SDZ and CDZ contain remarkably similar gouge layers, both of which consist of a clay-bearing, ultrafine grain matrix containing survivor clasts of sandstone and serpentinite. The two gouges have sharp boundary contacts with the adjacent rocks.

We have used X-ray Computed Tomography (XCT) imaging, at two different sampling resolutions, to investigate the mesoscale and microscale structure of the fault zone, specifically to characterize the shape, preferred orientation, and size distribution of the survivor clasts. Using various image processing techniques, survivor clast shape and

size are characterized in 3D by best-fit ellipsoids. Renderings of survivor clasts illustrate that survivor clasts have fine tips reminiscent of sigma type tails of porphyroclasts observed in myolonites. The resolution of the XCT imaging permits characterization of survivor clasts with equivalent spherical diameters greater than 0.63 mm. The survivor clast population in both the SDZ and CDZ gouge layers have similar particle size distributions (PSD) which fit a power law with a slope of approximately -3; aspect ratio (major to minor axis ratios) distributions also are similar throughout ranging between 1.5 and 4, with the majority occurring between 2-2.5. The volume- and shape- distributions vary little with position across the gouge zones. A strong shape preferred orientation (SPO) exists in both creeping zones. In both the SDZ and CDZ the minor axes form a SPO approximately normal to the plane of the San Andreas Fault (SAF), and the major axes define a lineation in the plane of the SAF.

The observation that the size-, shape- and orientation-distributions of mesoscale, matrix-supported clasts are similar in the SDZ and CDZ gouge layers, and vary little with position in each gouge layer, is consistent with the hypothesis that aseismic creep in the SDZ and CDZ is achieved by distributed, shearing.

The consistency between the SPO and simple-shear, strike-slip kinematics, and the marked difference of PSD, fabric, cohesion and clast lithology of the gouge with that of the adjacent rock, is consistent with the hypothesis that the vast majority of the shear displacement on the SAF at SAFOD is accommodated within the gouge layers and the gouge displays a mature, nearly steady-state structure.

DEDICATION

I dedicate this thesis to my grandfathers Dr. Harold Foerster and Thomas Sills. Pawpaw, you have inspired my academic and scientific endeavors over my lifetime, and for that I am truly grateful. Papa, your wisdom and guidance during my youth will never be forgotten.

ACKNOWLEDGEMENTS

First I would like to thank my committee chair, Dr. Judith Chester, for giving me the opportunity to work on this project. The support, guidance, and criticisms have helped me through this project and have made me a better scientist. I would also like to thank my committee member, Dr. Frederick Chester, for his wisdom and input throughout this project. Thank you to my outside committee member, Dr. David Schechter, for the use of his Petroleum Engineering Imaging Laboratory which was vital during the initial phases of this project.

Thanks also go to my friends within the Center for Tectonophysics, Charles, Hiroko, Caleb, Shay, and Bretani for the good times and support. Many thanks and gratitude to my best friend and roommate Clayton Coble for helping me scan the initial 36.6 meters of SAFOD core.

I also want to extend my gratitude to ExxonMobil Study Sponsorship Agreement #E-2008-ETC-009 for making the initial XCT imaging and analysis for this project possible. Thank you to the National Science Foundation NSF EAR-0643339 for the partial support of this research.

Thanks to all the family members who have supported me during this project, especially my mother.

Last, I would like to thank my beautiful girlfriend, Becca, for your patience, support and love.

TABLE OF CONTENTS

Page

LIST OF FIGURES

Page

LIST OF TABLES

1. INTRODUCTION

The mechanics of large-displacement faults is not well understood. There is increasing evidence that slip on large plate boundary faults occurs at extremely low levels of shear stress. Low levels of shear stress may be defined as stress that is less than expected based on the frictional properties of rock as determined from laboratory experiments [e.g. *Brune et al.*, 1969; *Byerlee*, 1978; *Lachenbruch and Sass*, 1980; 1992; *Zoback and Healy*, 1992; *Hickman and Zoback*, 2004; *Williams et al.*, 2004]. In addition, as illustrated by the San Andreas and other plate boundary faults, slip behavior varies between the end members of steady aseismic creep and episodic seismic slip in large earthquakes [e.g. *Sieh*, 1978; *Kanamori*, 1994; *Ando*, 2001; *Titus et al.*, 2006]. Why these faults are significantly weaker than the surrounding crust, what leads to localization of slip, and why some faults lock while others creep remain unanswered questions. A number of competing hypotheses have been put forward to explain the low shear strength [e.g. *Rice*, 1983; *Sleep and Blanpied*, 1992; *Chester et al.*, 1993; *Moore and Rymer*, 2007; *Collettini et al.*, 2009; *Schleicher et al.*, 2009a; *Schleicher et al.*, 2009b] and differences in mode of slip [e.g *Rice*, 1983; *Bos et al.*, 2000a; J*efferies et al.*, 2006a; *Jefferies et al.*, 2006b; *Hirono et al.*, 2008; *Collettini et al.*, 2009]. It is clear that advances in understanding the mechanics of faulting would be facilitated by documenting the structure and composition of faults, the role of fluids, and the underlying physical and chemical processes of deformation.

This thesis follows the style of *Journal of Geophysical Research.*

Numerous conceptual models describing the relationship between mode of fault-slip, fault structure and composition, mechanical properties, and mechanisms of slip have been developed. These models are based on experiments, theoretical models and field studies designed to understand frictional instability, dynamic rupture, fault structure, and deformation mechanisms [e.g. *Rice*, 1983; *Chester and Chester*, 1998; *Mair and Marone*, 1999; *Mizoguchi et al.*, 2009; *Kitajima et al.*, 2010]. A common hypothesis is that large displacement faults that slip seismically are characterized by rate-weakening frictional behavior and extreme localization of slip to millimeter scale zones of shear within much broader zones of damaged host rock [e.g. *Chester and Logan*, 1986; *Chester et al.*, 1993; *Chester and Chester*, 1998]. Observations of active faults at depth that are known to have slipped seismically tend to be consistent with the above hypothesis [e.g. *Ando*, 2001; *Tanaka et al.*, 2002; *Hirono et al.*, 2008]. In contrast, large-displacement faults undergoing aseismic creep are characterized by rate-strengthening behavior and distributed flow within thick (meter to decameter scale) zones of highly sheared gouge, cataclasite, and mylonites [e.g. *Rutter et al.*, 1986; *Bos et al.*, 2000b; *Faulkner et al.*, 2003; *Jefferies et al.*, 2006a]. This latter hypothesis has not been tested directly through study of actively creeping faults at depth. Successful drilling and core recovery from the San Andreas Fault Observatory at Depth (SAFOD) provides a unique opportunity to document the properties of a large-displacement fault undergoing aseismic creep in the brittle, upper crust.

The SAFOD is a 3-km deep scientific borehole that was drilled across the San Andreas Fault (SAF) near Parkfield, CA [e.g. *Hickman et al.*, 2004; *Zoback et al.*, 2010].

Scientific coring at SAFOD targeted the creeping segments of the fault zone at 2.5-3.0 km depth. Recovery of continuous spot core across two actively creeping traces of the fault zone demonstrate a correlation between the location of aseismic creep and the presence of distinct meters-thick layers of fault gouge [*Chester et al.*, 2008; *Zoback et al.*, 2010]. The two gouge zones are composed of a fairly homogeneous matrix of foliated, phyllosilicate-rich gouge that contains clasts of serpentinite and sedimentary rock derived from the surrounding host rocks [*Chester et al.*, 2008].

The purpose of this study is to better understand the processes of strain accumulation in the actively creeping zones of the SAF at SAFOD through study of the shape-, and orientation-distribution of mesoscale clasts in the two actively deforming gouge zones. The attributes of the clasts are documented through non-destructive X-ray Computed Tomography (XCT) and image analysis. We characterize the kinematics and homogeneity of strain at the mesoscopic scale, and interpret the processes of slip and flow behavior of the gouge. These data are compared to the fabric of other natural and laboratory-produced ductile shear zones, and to predictions from theoretical models [*Cladouhos*, 1999a; b; *Bos and Spiers*, 2001; *Pennacchioni et al.*, 2001]. By characterizing the mesoscale structure of the two actively creeping zones at SAFOD, this study can further develop current hypotheses relating the stability of slip, the localization of strain, and the role of flow processes in plate boundary faulting.

2. PREVIOUS WORK

2.1 Fault Zone Studies and Creep Mechanisms

Investigations of the mode of deformation within the gouge zones of exhumed, large displacement faults have revealed two general structural characteristics: extreme localization of slip and a composite planar fabric that is geometrically and kinematically similar to S-C fabrics in mylonitic shear zones [e.g *Chester and Logan*, 1986; *Rutter et al.*, 1986; *Chester et al.*, 1993; *Chester and Chester*, 1998]. Localization of shear at the mesoscopic scale is normally associated with frictional slip [e.g. *Chester and Chester*, 1998; *Chester et al.*, 2005; *Hirono et al*., 2008; *Isaacs et al.*, 2008] while mylonitic fabrics are normally associated with distributed flow [e.g. *Rutter et al.*, 1986; *Pennacchioni et al.*, 2001; *Jefferies et al.*, 2006a; *Jefferies et al.*, 2006b; *Chester et al.*, 2008].

In some cases, mesoscopic scale slip surfaces accommodate the vast majority of fault displacement [*Chester and Chester*, 1998]. Often these structures are interpreted to be products of coseismic slip and associated with dynamic velocity- or slip-weakening mechanisms [e.g. *Rice*, 1983; *Chester and Chester*, 1998; *Mair and Marone*, 1999; *Mizoguchi et al.*, 2009; *Kitajima et al.*, 2010]. Localization has been observed in many exhumed fault traces, including the Punchbowl [*Chester and Chester*, 1998] and San Gabriel Faults [*Chester et al.*, 1993], and at relatively shallow depths in seismically active faults, including the Nojima and Chelungpu Faults [e.g *Ando,* 2001; *Hirono et al.*, 2008].

A composite-planar, or S-C mylonitic fabric and more distributed deformation also have been observed in many exhumed faults. The Carboneras Fault, part of the Trans-Albora´n Shear Zone [*Larouziere et al.*, 1988], is a suggested analogue to the SAF at SAFOD where both creep and microearthquakes occur [*Faulkner et al.* 2003]. The phyllosilicate-rich gouge of the Carboneras Fault displays distributed deformation on anastomosing shear zones. Localization of slip is only observed along and within dolomite fault lenses. *Faulkner et al.* [2003] infered that the Carboneras Fault slipped aseismically in the phyllosilicate bearing shear zones, and by microearthquakes at slip surfaces in the dolomite lenses. The fault-bounded dolomite lenses within the anastomosing shears have aspect ratios ranging from 1 to 23, with the majority being 3 to 6 [*Keller et al.*, 1995]. The shape of the dolomite lenses is scale invariant over 30 km^2 to 3 m^2 [*Keller et al*., 1995]. The comparison of the shape of the dolomite lenses from *Keller et al.* [1995] will indicate that the shape of shear lenses, such as survivor clasts within the gouge at SAFOD, are scale invariant.

Many mechanisms have been associated with the creep in fault zones, several of which are associated with phyllosilicate-rich fault cores. Phyllosilicate minerals are weak during shear at elevated temperature and pressure conditions [*Bos and Spiers,* 2002; *Faulkner et al.*, 2003; *Solum and van der Pluijm*, 2004; *Solum et al.*, 2006].The fabric of the phyllosilicate-bearing gouge zones often are characterized by: 1) a P foliation, defined by the alignment of phyllosilicate minerals at approximately 135˚ to the master shear plane, 2) Riedel R1 shears, defined by the alignment of localized slip surfaces having a synthetic sense of shear and oriented at approximately 10-20° to the

master shear plane, 3) Riedel R2 shears, defined by the preferred orientation of localized slip surfaces having an antithetic sense of shear, and oriented at approximately 70-80° to the master shear plane, 4) Y shears, that are oriented parallel to the shear zone [*Rutter et al.*, 1986], and 5) crude shape fabrics defined by clasts of the host rock and compositional banding [e.g. *Chester et al.*, 1985; *Rutter et al.*, 1986; *Sibson*, 1986]. These structures are very similar to features in S-C mylonites that are typically associated with high temperature plastic flow [e.g. *Coble*, 1963; *Bell and Etheridge*, 1973; *Lister and Snoke*, 1984], even though the deformation mechanisms accommodating flow are different [*Chester et al.*, 1985]. For the high temperature creep, we expect grain boundary diffusion and with dislocation-aided creep to operate [e.g. *Coble*, 1963; *Bell and Etheridge*, 1973; *White*, 1976]. During lower temperature ductile flow we might expect cataclastic flow dissolution aided slip, and frictional sliding to dominate [e.g. *Borg et al.*, 1960; *Byerlee*, 1978; *Chester et al.*, 1985; *Bos et al.*, 2000b]. Therefore, we expect brittle homogenous flow at the mesoscopic scale across the creeping gouge zones at SAFOD because the temperature and pressures conditions at SAFOD are well within the regime of brittle deformation mechanisms [*Zoback et al.*, 2010], and the gouge contains abundant phyllosilicate minerals [*Solum et al.* 2006] which have been shown to deform by penetrative homogenous flow [*Rutter et al.*, 1986; *Bos and Spiers* 2001; *Faulkner et al.*, 2003].

2.2. Rigid Inclusions in a Viscous Matrix

Relatively few studies have focused on the kinematics of rigid inclusions within a brittle shear zone [e.g. *Cladouhos*, 1999a; b; *Hayman et al*., 2004]. For the case of simple shear of a viscous layer, two general types of models have been proposed: the *March* [1932] model and the *Ghosh and Ramberg* [1976] model. The March model assumes that the matrix and clasts within a shearing media are homogenous. In this case, the shape preferred orientation (SPO) of the clasts tracks with the finite strain ellipsoid, and the total shear strain that can be treated is limited (~ $\gamma = 8$) [*March*, 1932; *Cladouhos*, 1999a]. *Ghosh and Ramberg* [1976] consider the case of clasts rotating within a shear zone undergoing both pure shear and simple shear. In this scenario, the rate of rotation is governed by the ratio of the rate of pure to simple shear. To model only simple shear, the rate of pure shear is set to zero and the aspect ratio of the passive marker is assumed to be greater than the critical aspect ratio for stabilization. For simple shear only, the *Ghosh and Ramberg* [1976] model predicts that at large shear strains, e.g., $\gamma = 20$, the major axis of passive markers achieve their most stable position nearly parallel to the shear plane.

In brittle shear zones, where particle size reduction occurs by cataclasis, isolated, large clasts within a finer, granular matrix have been termed survivor clasts [*Sibson*, 1986; *Cladouhos*, 1999a]. *Cladouhos* [1999a] found that the SPO of clasts within the Death Valley Turtleback fault gouges were incompatible with the *March* [1932] and *Ghosh and Ramberg* [1976] model predictions for SPO. The SPO of clasts from the Death Valley Turtleback fault gouges had a major axis orientation approximately 135˚ to the master shear plane, whereas the model predictions for the *March* [1932] model

predicted a SPO approximately parallel to the master shear plane. The *Ghosh and Ramberg* [1976] model was incompatible because the ratio of the rate of pure to simple shear predicted a thickening shear zone. Cladouhos [1999a] concluded that shear zone thickening was unlikely over the lifetime of the fault zone. Therefore, a model considering inclined anisotropy, for example, one accounting for inclined shears and a penetrative clay foliation, was developed to explain the strain-insensitive SPO of the survivor clasts inferred from their field observations [*Cladouhos*, 1999a, b]. *Cladouhos* [1999b] concluded that either the SPO of the survivor clasts reflected low shear strain within the clay gouge, or that the long axes of the survivor clasts rotate to a strain insensitive position [*Cladouhos*, 1999b]. The SPO of the survivor clasts within the gouge zones at SAFOD will be compared to model predictions in order to analyze the geometry and kinematics of the gouge zones.

2.3 State of Stress and Friction along the San Andreas Fault

The maximum horizontal compressive stress, S_{Hmax}, along the SAF has been determined to range 60-90° to the fault plane. The observed regional stress orientations are greater than those predicted by Andersonian theory of faulting, where S_{Hmax} is predicted to be 30° to the fault plane [*Anderson,* 1951]. Mount and Suppe [1987] noted that the orientation of the borehole elongations and breakouts, folds, and thrust faults adjacent to the SAF implied S_{Hmax} was oriented at 84° to the fault plane. The orientation of S_{Hmax} approximately perpendicular to the SAF was further constrained by borehole breakout orientations near the SAF at Cajon Pass, CA [*Zoback and Healy*, 1992]. At

SAFOD, the orientation of S_{Hmax} approximately normal to the SAF has been observed through borehole breakout orientations from the SAFOD pilot hole [*Hickman et al.*, 2004], and by geophysical data at SAFOD [*Boness and Zoback*, 2004]. Recently core studies from Phase 1, at SAFOD, have indicated that conjugate fracture orientations are consistent with an S_{Hmax} that is orientation nearly perpendicular to the SAF [*Almieda,* 2007]. Subsidiary faults along San Gabriel Fault, an extinct exhumed trace of the SAF, display preferred orientations consistent with a conjugate geometry, in which the bisector and the inferred orientation S_{Hmax} is oriented 60° to the fault plane [*Chester et al.* 1993]. A study of microfractures in the Punchbowl Formation by *Wilson et al.* [2003] indicates that opening-mode fractures near the fault into the outer damage zone also demonstrate that the S_{Hmax} was oriented nearly perpendicular to the fault plane.

A lack of a heat flow anomaly adjacent to the SAF [e.g. *Brune et al.*, 1969, *Lachenbruch and Sass*, 1980; 1992] coupled with the observed orientation of S_{Hmax} requires that the SAF to be weak in an absolute sense. At the current heat flow conditions, the coefficient of friction required for frictional failure would be less than 0.2 [*Lachenbruch and Sass*, 1980; 1992]. This contrasts the predicted frictional strength of most earth materials, 0.7 [*Byerlee*, 1978], leading to the conclusion the SAF is weak in an absolute sense.

3. DESCRIPTION OF STUDY AREA

3.1. The San Andreas Fault at SAFOD

The SAF forms a right-lateral, transform boundary between the North American and Pacific plates [*Atwater, 1970 and 1989*]. The fault is composed of two locked segments, one North of San Juan Batista that extends northward to the Mendicino Triple Junction, and a second that is located South of Gold Hill, CA. Between the locked segments the plates move past each other at an average rate of 2.5 cm/yr [*Titus et al.,* 2006]. The majority of fault displacement in the central region is accommodated by aseismic creep accentuated by numerous small (M5 and smaller) and often repeating earthquakes that occur on stationary patches of the fault plane (Figure 1) [*Hickman et al.*, 2004; *Thurber et al.*, 2004]. The stationary patches are relatively small, accounting for approximately 1 percent of the total area of the fault plane [*Zoback et al.*, 2010]. To address fundamental questions about earthquake processes along a major plate-boundary fault, a 3.2 km deep borehole, SAFOD, was drilled across the SAF at the southern end of the creeping section near Parkfield, CA. Currently, this borehole remains open for continued scientific study. This borehole offers an excellent opportunity to study an actively creeping, and important section of a major plate boundary fault.

3.2 Structure of the SAF at SAFOD

Drilling at SAFOD began with a vertical pilot hole, followed by two phases of directional drilling and coring to complete the main hole, and a third phase of

multilateral drilling and coring off of the main borehole. The main hole is vertical to a depth of approximately 1.5 km, and then inclined 50-60˚ to the Northeast, crossing the SAF at about 3 km depth (Figure 2) [*Zoback et al.*, 2010]. Prior to coring Phase 3, caliper logs of the main borehole recorded active casing deformation at 3192 m measured depth (MD) and 3302 m MD. The casing deformation reflects actively creeping portions of the SAF intersected by the borehole. The two deforming zones recorded by the caliper logs are referred to as the Southwest Deforming Zone (SDZ) at 3192 m MD and the Central Deforming Zone (CDZ) at 3302 m MD [*Zoback et al*., 2010]. Coring at SAFOD successfully sampled 1) a granodiorite and two arkosic sandstones of the damage host rocks bounding the west side of the SAF, 2) the fault core associated with the SDZ, which consists of a foliated gouge and foliated cataclasites that bound the gouge on the west side, and deformed interbedded siltstones and sandstones that bound the gouge on the east, and 3) the foliated gouge containing the CDZ [*Chester et al.,* 2008].

At the mesoscale, the gouge samples from the two active creeping traces (SDZ and CDZ) are remarkably similar [*Chester et al.*, 2007; *Chester et al.*, 2008]. Both are composed of ultrafine-grained, sheared serpentinite-rich gouge that contains clasts of surrounding host rocks, including serpentinite, sedimentary rocks, and cataclasites. Most of the clasts captured in the cored intervals are less than 10 mm in length; however, the presence of larger clasts is demonstrated by a 30 cm-wide serpentinite block displayed near the top of the foliated gouge associated with the SDZ [*Chester et al.*, 2008]. The serpentine block is bounded by faults on both sides. The western fault contact is sharp,

whereas the eastern contact is a few cm-wide serpentinite shear zone. The foliated gouge of the SDZ at this location is between 1.3 to 2.1 meters wide, and that associated with the CDZ is about 2.5 m wide [*Chester et al.*, 2008].

Our study specifically targets the gouge of the SDZ and CDZ to investigate the structure of actively deforming fault gouge at 2 to 3 km depth (Table 1).Using core acquired from these two zones, we characterize the mesoscale structure of the 1) foliated gouge, foliated cataclasites, and sheared interbedded sedimentary rocks associated with the SDZ, and 2) foliated gouge associated with the CDZ.

3.3. Geographic Orientation of Core Samples

Geophysical logging of the Phase 3 borehole could not be completed as a result of hole collapse and loss of the logging tool. As a result, the Formation Microimager Log (FMI), which could have been used to orient the Phase 3 core, was not acquired. Accordingly, the orientation of the core samples, with respect to the geographic reference frame, was determined using log data from Phase 2 [*J.S. Chester and F.M. Chester*, 2010 Personal Communication]. The position of the core samples in the borehole can be determined by aligning bedding, and prominent fractures, to specific features and fabrics imaged by the GeoVision resistivity (GVR) logs and in the Baker Atlas STAR ImagerTM (STAR) logs (Table 2). To date, all of the Phase 3 core samples have been oriented except for the samples from the CDZ [*J.S. Chester and F.M. Chester*, 2010 Personal Communication].

4. METHODS

4.1. X-ray Computed Tomography (XCT) Scanning

X-ray computed tomography (XCT) imaging is a useful tool for imaging objects in both the medical and manufacturing industries over the past few decades [*Ketcham and Carlson*, 2001]. XCT imaging offers a non-destructive technique to investigate objects in three-dimensions. For medical XCT scanners, X-rays are emitted from a source around the stationary object to be imaged and captured by detectors. For industrial XCT scanners, the X-ray source and detectors remain stationary and the object to be imaged rotates in the path of the X-rays. Since the imaged object or the source and detectors rotate, the X-ray attenuation yields multiple orientations of the material in the object. X-ray attenuation can be defined as the decrease in photons when the X-rays intersect a material substance. Attenuation is directly related to the density of the material that the X-rays are passing through [*Ketcham and Carlson*, 2001]. The data collected from the detectors are then used to create an image slice. The image slices are reconstructed by converting sonograms into two-dimensional images. The images of the sonogram are then assigned a XCT value based on the amount of X-ray attenuation, in which case the XCT value is referred to as the radiodensity [*Novelline* 2004]. Henceforth, we referred to the assigned XCT value as the radiodensity. In the reconstructed image slices, the radiodensity corresponds to the gray value at that particular pixel. The brighter or higher the radiodensity, the greater the density, whereas the darker or lower the radiodensity the lower the density. The radiodensity values must

be calibrated in relationship to a particular material, often saline water, in which the radiodensity, called the Hounsfield Unit (HU), is known [*Ketcham and Carlson*, 2001]. The radiodenisty values of the slices can then be compiled to create a 3D image of the object being studied. The radiodensity values in the 2D slices are averaged to create a voxel [*Ketcham and Carlson*, 2001]. A voxel can be described as a cubic or rectangular representation of a pixel. The size of the voxel is dependent on the resolution and spacing of the image slice. The resulting 3D image can then be used to gather non-destructive qualitative and quantitative data.

We acquired low resolution images at the Harold Vance Department of Petroleum Engineering X-Ray Computed Tomography Facility at Texas A&M University. This system utilizes a Universal Systems hd-350e CT scanner [*Kim et al*., 2006] that can accommodate rock core up to 10.2 cm in diameter and 1 m in length. All core collected during Phase 3 drilling, was scanned at 130 kV and 100 mA, and a slice spacing of 2 mm. Each scan has an image resolution of 512 x 512 pixels, and yields a voxel element that is 0.25 mm x 0.25 mm x 2 mm.

High-resolution images were acquired at the X-ray Computed Tomography Facility of The University of Texas at Austin (UTCT) using an ACTIS scanner [*Huddlestone-Holmes and Ketcham* 2010]. Two intervals (3297.1-3297.2 m MD, and 3298.1-3298.2 m MD) that represent the structure of the gouge in the CDZ were scanned at 450kV and 1.3 mA. Each scan has an image resolution of 1024 x 1024 pixels, and yields a voxel element that is 0.118 mm x 0.118 x 0.25 mm. The images were processed

by the XCT operator at the UTCT facility to remove noise, including beam hardening and rings e.g., [*Ketcham and Carlson*, 2001].

4.2. Image Analysis

A combination of manual and automated techniques were used to process the XCT image stacks, render the structure of the core in 3D and 2D orthographic projections, and quantify the size-, shape-, and orientation of each clast, as well as identify and determine the orientation of other structural features.

ImageJ and Graphic Converter were used to improve the image quality by correcting for uneven illumination. To characterize the size, shape, and orientation of the clasts, the gray-scale images were converted to binary images to distinguish the clasts from the matrix (Figure 3a). The binary images were then manually processed to remove the core sleeves, truncated clasts, and noise to facilitate automated analysis performed using Blob3D [*Ketcham*, 2005].

Blob3D [*Ketcham,* 2005] identifies a clast by connecting voxels that are within a specified density range (Figure 3b) and then determines the total volume of the clasts. Using this volume the best-fitting ellipsoid is determined. Output data include the position, volume, lengths of the major, minor and intermediate axes, and orientations of these axes for each clast in the core reference frame.

The orientation distribution of the clasts was determined by plotting the major and minor axes of each clast in lower hemisphere equal area projections and analyzing the orientation distribution using Stereonet, a freeware program provided by R. W.

Allmendinger [http://www.geo.cornell.edu/geology/faculty/RWA/programs.html]. The position, size and orientation of other structures, particularly planar fabric elements such as fractures, layering, veins, and shears, were measured from the image sequences using the OsiriX imaging software and DICOM viewer (Figure 4). Two-dimensional orthographic projections of the image stacks were used to search for structures and make orientation measurements in the slice view i.e. (projection plane oriented perpendicular to the core axis) and two slab views i.e. (two orthogonal projection planes oriented parallel to the core axis). In the core coordinate system, the orientation of planar objects is defined by the orientation of the plane in the slice view (the "strike") and the inclination of the plane in a slab view (an "apparent dip").

The size of each is represented by the diameter of a sphere that has a volume equal to that given by Blob3D. The particle size distribution will be analyzed using cumulative frequency plot, specifically to determine if the data fit a power law distribution [e.g. *Sammis et al.*, 1987; *Bonnet et al.,* 2001]. If so, we define the minimum statistically significant clast size by the truncation effect [*Bonnet et al.,* 2001]. This analysis identifies the smallest clast size that one can effectively sample given the image resolution. The maximum statistically significant survivor clast size will be determined by the censoring effect; this will define particles that are too large to be effectively sampled by the 101.6 mm diameter core [*Bonnet et al.*, 2001].

Analysis of the shape distribution is facilitated by the use of the Flinn diagram and the aspect ratio of clasts.

5. RESULTS

5.1 Mesoscale Characteristics of the Cored Intervals

5.1.1 SDZ and CDZ gouge zones

The survivor clasts within the SDZ and CDZ gouges are matrix supported. The XCT radiodensity of the gouge matrix is lower than that of the entrained survivor clasts (Table 3). Open fractures cutting the gouge matrix and clasts, and missing sections of core are distinguished by extremely low XCT radiodensity and appear black in images (Table 3). Some survivor clasts show evidence of pronounced intraclast fracturing in the high resolution XCT images. Extremely high XCT radiodensity elements within and at the boundaries of survivor clasts are distinguishable in both low and high resolution images. These elements probably correspond to fracture filling by the iron-bearing minerals, pyrite and chalcopyrite, and calcium-bearing minerals such as calcite.

5.1.2 Foliated cataclasite west of the SDZ

The foliated cataclasites are defined by millimeter-thick layers that are distinguished by contrasting XCT radiodensity (Figure 5a). In some sections of the foliated cataclasite, networks of small veins displaying one or two distinct preferred orientations are obvious because of the higher radiodensity of the vein-filling phase. Small shears that have lower radiodensities than the surrounding matrix are also present and display preferred orientations. Distinct clasts are present within portions of the foliated cataclsites. These clasts are similar to those noted in the two foliated gouge in

that they have higher XCT radiodensities than the surrounding cataclasite matrix and are cut by open and mineral-filled fractures (Figure 5a and Table 3).

5.1.3 Interbedded sandstone and siltstones

The sheared interbedded sandstone and siltstones bordering the east side of the SDZ gouge are composed of thinly bedded shales that strike nearly orthogonal to the core axis, and 4 interbedded siltstone and sandstone blocks. The siltstone and sandstone units are cut by two distinct system of faults. In addition, the sandstone displays pinch-and-swell structures illustrating that boudinage has taken place (Figure 5b). The sandstone boudins are cut by numerous veins which are parallel to the core axis. The veins have a higher radiodensity than the siltstone and sandstone, and the siltstone and sandstone layers have a higher radiodensity than the shale layers (Table 3).

5.1.4 Massive shale

The massive shale has a low XCT radiodensity (Figure 6 and Table 3). The shale is cut by numerous small veins which are distinguished by a higher XCT radiodensity compared to the surrounding matrix (Table 6). The veins are 1 to 2 cm in length in slab view and can be less than 1 cm in length in the slice view.

5.2 Size, Shape, and Orientation Distribution of Clasts in the Southwest Deforming Zone Gouge

5.2.1 Shape and size distribution of clasts

The 159 largest clasts imaged in the foliated gouge of the SDZ range in size from 4 to 30 mm in diameter. The distributions of clast size on the western and eastern sides

of the serpentinite block are similar (Figure 7a). The size distribution of the 159 clasts is best described by a power law

$$N(D)/L = aD^n$$

with n=-3.3 over the size range 6.42 mm < D < 27.7 mm, where D is the equivalent spherical diameter of clasts, N(D/L) is the cumulative number of clasts with size greater than D, L is the length of the core interval in which clasts were counted, and a and n are constants (Figure 7b). Imaged particles smaller than 6.4 mm and larger than 27.7 mm deviate from the power law relationship because of truncation and censoring effects, respectively [*Sammis et al.,* 1987; *Bonnet et al.,* 2001].

Within the CT image views and 3D renderings, clasts range in shape from sub-rounded ellipsoids to phacoids; however, the low-resolution of the images masks angular boundaries and phacoidal shapes of the smaller clasts; this likely makes the clasts appear more rounded than they actually are. The clasts have aspect ratios (i.e., the length ratio of the major axis to minor axis) between 1 and 4, and the distribution of aspect ratios is similar on both sides of the serpentinite block (Figure 8). The aspect ratios of the majority (greater than 70%) of all clasts are 1.5 to 2.5. The shapes of the clasts, as determined from the best-fitting ellipsoids by Blob3D, generally are scalene in shape, i.e., the intermediate axis is different than both the major and minor axes (Figure 9). Although scalene ellipsoids approximately similar in shape to both prolate and oblate spheroids are present, the majority of ellipsoids have intermediate axis lengths that are

closer to the major axis lengths than to the minor axis lengths, i.e., approach the shape of an oblate spheroid rather than a prolate spheroid.

The clasts within the gouge on both sides of the serpentinite block display a distinct shape preferred orientation, SPO (Figure 10). Specifically, the major and minor axes of the clasts form very diffuse great circle girdles, each containing a point concentration. Using the geographic orientation of this cored interval (Table 2), we find that the average orientation of the minor axes, defined by the point maximum, is approximately horizontal and trends perpendicular to the strike of the plane of the SAF. The point maximum defined by the major axes is approximately horizontal and parallel to the strike of the SAF (Figure 10). Assuming a Bingham distribution, the best-fit plane containing the major and intermediate axes of all clasts associated with the SDZ strikes parallel to the SAF but dips steeply to the northeast, opposite to the dip direction of the SAF. The best-fit plane is approximately parallel to the western gouge/serpentinite contact and to the foliation in the foliated cataclasites (Figure 10).

5.3 Size, Shape, and Orientation Distribution of Clasts in Central Deforming Zone Gouge

5.3.1 Shape and size distribution of clasts

For the foliated gouge associated with the CDZ, the low resolution XCT images define clasts with an equivalent spherical diameter between 59.8 to 6.3 mm, and the high resolution scans define clasts with diameters between 19.9 and 0.63 mm. Combining the equivalent spherical volumes for all clasts analyzed in the low resolution scans, we

estimate a total clast volume for this gouge of 1.863 x 10^6 mm^3. This amounts to approximately 10% of the total gouge volume for the foliated gouge from the CDZ. Using the combined high- and low-resolution image data, the volume and three-dimensional shape of 6447 clasts were determined. The size distribution is adequately described by a power law for clasts between 1.26 and 16.2 mm in diameter (Figure 11). Imaged particles smaller than 1.26 mm and larger than 16.2 mm deviate from the power law relation as expected for truncation and censoring effects, respectively [Sammis et al., 1987; Bonnet et al., 2001]. The exponent of the best-fit power law is -3.0. The distribution of clasts with equivalent spherical diameters between 8.0 mm to 16.2 mm is nearly uniform throughout the gouge (Figure 12 d, e).

As in the SDZ, at low resolution the shapes of the clasts appear as sub-rounded ellipsoids to phacoids. At high resolution, however, it is clear that the boundaries of clasts are not always well-defined in the low resolution images. Many clasts have lenticular fish-shapes (Figure 13) that are characterized by acute-angle, very delicate tips at the edges of the clasts (Figure 14). Overall, the clasts have aspect ratios between 1 and 4 (Figure 12 a-c), and the majority (greater than 70%) of all clasts have an aspect ratio between 1.5 to 2.5. The local distribution of clast shapes does not vary significantly with position across the gouge layer (Figure 12 a-c). To first order approximation, the clasts are best-fit by scalene ellipsoids; a slightly greater proportion of clasts have intermediate axes that approach the major axis length rather than the minor axis length, i.e. they appear more like oblate than prolate shapes (Figure 15).

Similar to that seen in the SDZ, the clasts in the CDZ have strong shape-preferred orientations. In stereographic projections, the long axes of clasts form a great-circle girdle pattern that contains a point maximum, and the short axes of clasts tend to form a strong point-maximum (Figure 17). Unlike the case for the SWZ gouge zone, there is no independent information at this time to orient the core from the CDZ to a geographic frame of reference, i.e., the angle of rotation about the core axis is unknown. By analogy with the fabric of clasts in the CDZ, we assume the point maximum defined by the long axes of clasts is horizontal, and determine the angle of rotation of the core about the core axis (Table 1). With this assumption, there are two possible rotations, different by 180˚, that align the point maximum to horizontal. For both cases the girdle defined by the long axes strikes approximately parallel to the macroscopic orientation of the San Andreas Fault and dips towards the southwest, i.e., the girdle is approximately coplanar with the San Andreas Fault. One rotation angle gives a dip magnitude of approximately 70˚, and the other rotation angle gives a dip of approximately 40˚. Given that the San Andreas Fault at SAFOD is generally assumed to dip 83˚ SW, we have used the rotation angle that results in the steeper dip of the long-axis girdle when plotting orientation data of the CDZ.

In stereographic projections, the orientation of the major axes of clasts, as a function of aspect ratio, displays a great-circle girdle pattern (Figure 16). The girdle is diffuse for clasts having low aspect ratios (less than 1.5) and much more concentrated for clasts with aspect ratios from 1.5 to 4. In some cases the major axes define a point

concentration superposed over the girdle distribution. This point concentration is less pronounced as the aspect ratio increases.

In stereographic projections, the orientations of the major axes of the clasts, plotted as a function of clast size display a great circle girdle containing a point maximum, and the minor axes define a point maximum (Figure 17). In general, there is little difference in fabric for different clast size ranges, i.e., the shape preferred orientation of clasts is invariant with respect to clast size.

5.4. Fabric of the Foliated Cataclasites in the Southwest Deforming Zone

5.4.1 Orientation of layering, veins, and shear zones

The foliation in the foliated cataclasite west of the SDZ is defined by contrasting radiodensities. The poles to the foliation are shown in two figures because the foliated cataclasite west of the SDZ is contiguous through two coring sections; the two figures illustrate the contiguity of the foliations throughout the core section breaks. These orientations are the essentially the same indicating that the two section are contiguous. Overall, the average orientation of the foliation is 355, 88 E (Figure 18a). The foliation is oblique (~45°) to the strike of the SAF.

The veins cutting the massive shale form two distinct sets that are defined by a large dihedral angle. The poles to the dominant set forms a strong point concentration defining a veins that are sub-vertical and oriented approximately 45° to the SAF. The weaker set is defined by a plane that is dipping approximately 51° degrees to the north and is 45° degrees to the SAF. Together these veins define a large dihedral orthogonal

angle to one another, where the orientation of major set is 006.8, 79.7 E, and the orientation of the minor set is 266.6, 51.4 N, and the bisector of the two veins is approximately 90° to the macroscopic orientation of the SAF. The orientation of the layering of the foliated cataclasite (302, 61 N) adjacent to the massive shale, and the SDZ foliated gouge strike parallel to the SAF and dip steeply to the northeast, opposite to that of the SAF (Figure 20a).

5.4.2 Shape, size and orientation distribution of survivor clasts

The largest clast wholly contained within the core of the foliated cataclasites west of the SDZ has an equivalent spherical diameter of 20.2 mm. The three dimensional shape of 39 clasts was determined using the low resolution XCT images (Figure 19b).

The aspect ratios of the clasts vary between 1.5 and 5 (Figure 19a). The majority (greater than 70%) of all clasts have aspect ratios from 1.5 to 3.5.

The clasts in cataclasites display strong shape preferred orientations (Figure 18c) similar to the orientation of clasts in the SDZ and CDZ foliated gouges. The major and minor axes of the clasts form diffuse girdles containing a point concentration. Using the geographic orientation of this cored interval (Table 2), we find that the point maxima of the minor axes is approximately horizontal and perpendicular to the average orientation of the foliations. The point maxima defined by the major axes is oblique (~45°) to the strike of the SAF. Assuming a Bingham distribution, the best-fit plane containing the major and intermediate axes of the clasts dips steeply to the east.

5.4.3 Orientation of layering, veins and shears in the interbedded sandstones and siltstones

The orientation of the shale layering is 334, 88 SW (Figure 20c). The veins within the siltstone blocks have two distinct orientations. The dominant vein set is oriented 37, 68 E, and strikes nearly perpendicular to the macroscopic orientation of the SAF, and has a steep dip to the southeast. The minor vein set is oriented 297, 37 N, strikes approximately parallel to the SAF, and has a shallow dip to the northeast. Two prominent shears cut through the lower siltstone block. Both shears have right lateral displacement defined by the relative offset by markers such as veins and layering. The orientation of shear 1 is 353, 78 E and the orientation of shear 2 is 20, 81 E. The two shears strike 69° and 44° to the macroscopic SAF, respectively, with a synthetic shear sense.

6. DISCUSSION

6.1. Homogeneity of Deformation in the Gouge Zones

The structure of the foliated gouge is remarkably similar within and between the SDZ and CDZ. Clasts in both zones are matrix supported, phacoidal in shape with similar aspect ratios. Also, the shape preferred orientation of clasts in both gouge zones is similar in that the preferred orientation of the short axes are approximately perpendicular to the macroscopic orientation of the SAF. The size distribution of survivor clasts is fractal, and the scaling relationship is similar, for both gouge zones. The similarity suggests that both gouge zones were formed at similar conditions and both reflect a similar, large magnitude of shear strain.

The lack of a spatial variation in the size distribution, shape, and preferred orientation of clasts within the foliated gouge of the CDZ is consistent with a homogeneous distribution of strain across the gouge. In general, for low-temperature shear zones, particle size reduction is associated with an increase in shear strain, and the shape and preferred orientation of clasts vary with magnitude and orientation of strain [e.g. *Sibson,* 1977; *Rutter et al.* 1986]. If strain had been localized within the gouge, we would expect to observe a variation in the size and fabric of the clasts with respect to position. However, we find no evidence to suggest extreme localization occurred at the mesoscopic scale in either of the two gouge zones.

Our observation of scale independence in shape is consistent with the shape and size distribution of shear lenses studied by *Keller et al.* [1995]. Although the lenses of

dolomite in the Carboneras fault are not matrix supported, the geometry of the lenses determined through mapping are consistent with phacoidal shapes. The aspect ratios of the lenses range from 1 to 23, though the majority of the ratios are 3 to 6. *Keller et al.* [1995] found that the shape of the lenses is scale invariant over 30 km^2 to 3 m^2. The SPO of clasts in the brittle shear zones described by Cladouhos [1999a] also appear scale-invariant over several orders of magnitude.

The finding that the deformation in the foliated gouge zones is homogeneous, at least at the mesoscopic scale, supports the hypothesis that aseismic creep is associated with distributed, shearing flow within gouge layers. Homogenous distribution of deformation has been noted in some exhumed fault zones, such as the Carboneras Fault, Keumwang fault zone, and Median Tectonic Line, MTL [e.g. *Rutter et al.*, 1986; *Faulkner et al.,* 2003; *Lee and Kim,* 2005; *Jefferies et al.,* 2006]. In all cases, the shear zones are predominately composed of phyllosilicate rich fault gouges similar to SDZ and CDZ foliated fault gouges. The shear strain in the MTL, Carboneras, and Keumwang faults is achieved by slip on pervasive shears of P-, Y-, and R1- orientations throughout the phyllosilicate rich gouge zones. Observations of the core section from the SDZ that was split open axially to expose the interior portions of the foliated gouge displayed many striated and polished surfaces. In addition, the high-resolution XCT images display pervasive parting along foliation in the gouge. Thus the fabric of the foliated gouge from the SDZ and CDZ is similar to the characteristics of phyllosilicate gouge from other faults, and supports interpretations that these types of fabrics are associated with aseismic creep [*Faulkner et al.,* 2003].

6.2. Kinematics of Deformation in Core of SAF

The core sections from the SDZ and CDZ display distinct transitions in fabric at the boundaries of the gouge zones that reflect different magnitudes and orientations of strain. The SPO of the clasts in the gouge zones in which the short axes of the clasts are perpendicular to the shearing plane, is similar to the fabrics of clasts observed in both brittle and ductile shear zones with large shear strain. The SPO of the survivor clasts within the SDZ and CDZ is consistent with orientations of clasts in the Death Valley detachment faults associated with transtension of the Eastern California Shear Zone [*Hayman et al.,* 2004]. The clasts have scalene to oblate ellipsoid shapes and the short axes of clasts are perpendicular to the shear plane [*Hayman et al*. 2004]. Sillimanite clasts from ductile shear zones also display a similar SPO in which the long axes of the sillimanite porphyroclasts are subparallel to the master shear zone, and the minor axes from a strong SPO perpendicular to the shear zone [*Pennacchioni et al.* 2001]. A similar SPO of clasts is produce within a phyllosilicate gouge, deformed to very high shear strains ($> \gamma=130$) in rotary shear experiments [*Bos et al.*, 2001]. The structure in all the shear zones recorded by the survivor clasts is consistent with numerical- and kinematic models derived for simple-shear in which the short and long axes of a population of survivor clasts achieve a near steady-state orientation approximately perpendicular and parallel to the shear zone, respectively. The *Ghosh and Ramberg* [1976] model for simple shear predicts that at large shear strains, e.g., $\gamma < 20$, the major axis of passive markers achieve their most stable position nearly parallel with the shear plane.

The low volume fraction of clasts (~10%), and the scaling relations for clast size and frequency as indicated by the slope of the PSDs for both SDZ and CDZ foliated gouge indicates that both gouge zones are mature, large shear strain zones. The slope of the PSD in log number versus log dimension plots of approximately 3 for the PSDs from the SDZ and CDZ foliated fault gouge are in good agreement with the PSDs of exhumed fault core where large amounts of displacement and extensive comminution have occurred [e.g. *An and Sammis*, 1994; *Billi,* 2007]. They also agree with the upper bounds of theoretical D values for high strain shear zones [*Sammis et al.,* 1987]. Together the PSDs and low volume of clasts suggests that the SDZ gouge and CDZ gouge have both experienced huge strains.

In the case of the CDZ, the shape fabrics may be oriented with respect to the geographic reference (table 2), and the SPO are consistent with pure strike-slip movement along the SAF at SAFOD (Figure 10 and 17). GPS data over the past few decades indicates that the major component of slip is pure strike-slip along the SAF at the creeping section [*Argus and Gordon* 2001; *Titus et al.* 2005], and that only approximately 1 km of net vertical motion has occurred over the last 60 Ma along the SAF in the vicinity of SAFOD [*Bylthe et al.* 2004]. New cross sections through the SAFOD drilling site, using cuttings [*Bradbury et al.* 2004] and high-resolution seismic reflection data [Rymer et al. 2004], interpreted the fault zone bounded to the East and West by nearly vertical faults which is consistent with strike-slip kinematics. The structure of the SDZ and CDZ foliated gouges, as recorded by the orientation

distributions of survivor clasts with the long axes of clasts preferentially oriented horizontal, are consistent with simple-shear kinematics and strike-slip faulting.

The structure of the neighboring rock adjacent to the SDZ record smaller strain magnitudes, and shear directions oblique to the shear direction of the SAF. The different strain orientations are inconsistent with the simple-shear kinematics and strike-slip faulting in the gouge and the lithology of the rocks are somewhat different than those in the foliated fault gouge for the SDZ and CDZ (Table 1). The foliated cataclasites directly adjacent to the SDZ gouge display a foliation that is subparallel to the gouge zone, which suggests this cataclasite is associated with the latest stages of displacement of the SDZ. Subparallel orientation of the foliation in the cataclasite adjacent to the SDZ is generally observed in well-preserved exhumed faults [e.g. *Chester et al.* 1993]. In contrast, foliations in the foliated cataclasite (Figure 18 a and b), 3186.71-3193.8 m MD, further from the SDZ gouge zone are oblique to the gouge zone and thus were formed earlier and were subsequently offset and rotated on subsidiary faults. This interpretation is based on the different orientation of the cataclasite unit directly adjacent to the SDZ gouge (subparallel to the SDZ) and the foliation of the cataclasites from 3186.7-3193.8 m MD that is not subparallel to the SDZ gouge contacts or that of the macroscopic orientation of the SAF.

Orientation distribution of the small veins within the massive shales (Figure 26) and the veins, shears, and boudinage within the sheared interbedded siltstones and shale (Figure 20c) may be related to the approximate perpendicular shortening of the SDZ gouge zone and to the SAF. The shortening direction is consistent with those observed

from exhumed fault [*Chester et al.,* 1993; *Wilson et al.,* 2003], and the stress orientations in the damage zone at SAFOD and regional structures around the SAF [e.g. *Mount and Suppe,* 1987; *Hickman and Zoback,* 2004; *Boness and Zoback* 2004; *Almeida,* 2007]. Preservation of these features implies little shear occurred in the bounding rocks relative to that within the gouge layers. We infer that the two gouge zones represent the meters thick zones in which the majority is shear displacement occurs.

6.3. Flow Processes in the Gouge Layer

Lenticular, phacoidal shapes of the clasts in the SDZ and CDZ suggest that the rotation of clast occurs at slower rates relative to those of surface shaping processes. If rotation of the survivor clasts within the SDZ and CDZ foliated gouges occurred at higher relative rates than the shaping processes, we would expect rounded more prolate ellipsoidal shapes. *Cladouhos* [1999] noted that penetrative strain in phyllosilicate rich fault gouge can stabilize and slow the rotation of survivor clasts. *Pennacchioni et al.* [2001] also noted that the population of porphyroclasts within the extensional crenulation cleavage (ECC) of ductile mylonites displayed a nearly steady state orientation. Strong SPO and the lenticular shapes of the clasts within the SDZ and CDZ foliated gouge suggest that clasts are oriented along penetrative shear surfaces.

The lenticular shapes of the clasts in the gouge, and the acute-angle, sharp-tipped edges of many clasts support the interpretation that reduction of clast size occurs by mechanical and chemical surface-shaping processes rather than intraclast fracture or flow. Lenticular fish shaped halite porphyroclasts have been produced in experiments

[*Bos and Spiers*, 2001]. *Bos and Spiers* [2001] experiments were conducted at conditions where frictional and time dependant chemical reaction deformation processes would be operative. *Bos and Spiers* [2001] concluded that cataclasis was the dominant deformation mechanisms reducing the porphyroclasts size during the onset of the experiments, and that frictional wear processes were dominant, but pressure dissolution were probably active in shaping the halite porphyroclasts in the later stages of the experiments.

Serpentine gouge experiments have produced crystallographic preferred orientations of serpentine grains and distributed deformation [*Reinen,* 2000]. *Reinen* [2000] experiments were conducted at room temperature conditions were brittle deformation processes such as frictional slip on discrete surfaces where cataclasitic flow would dominate. *Reinen* [2000] suggested the serpentine crystals rotated into a crystallographic orientation. Experimentally deformed serpentine gouge displayed rate-strengthening behavior and distributed deformation. *Reinen* [2000] implied that distributed deformation was associated with stable sliding and aseismic creep.

PSDs from the SDZ and CDZ foliated fault gouge suggests that this maturity of the gouge is similar to that observed in the Punchbowl and San Gabriel ultracataclasites [*Chester et al.,* 1993; *Chester et al.,* 2005]. The mechanical significance of the D value implies that fracturing by the similar sized nearest neighbor particles is no longer the dominant clast size reduction mechanism. Grinding of clast boundaries by similarly hard or harder particles entrained within the fault gouge is the dominant mechanism [*Sammis et al.,* 1987, *Chester et al.,* 2005].

The matrix of the foliated fault gouge is incohesive throughout the gouge [*Chester et al.*, 2008]. The incohesive nature of the gouge suggests large amounts of displacement have occurred, and constant aseismic creep has prevented cementation and healing of the pervasive distributed shear surfaces within the SDZ and CDZ gouges [e.g. *Chester and Logan*, 1986; *Chester et al.*, 1993; *Chester and Chester*, 1998].

The incohesive nature of the gouge matrix suggests microscopic fracture and interparticle sliding are the dominant microscale deformation processes. At the depth and pressure regimes for the SDZ and CDZ foliated gouges, frictional processes such as spalling, chipping, and granular wearing of surfaces should be dominant [*Sibson*, 1977]. Apparent stability of lenticular clasts aligned parallel to the gouge layer suggests contacts between matrix and clasts are best described as frictional slip surfaces. If the clast population maintains a nearly steady-state orientation within a distributed shearing matrix, frictional slip along the boundaries of survivor clast probably occurs. Clast shapes indicate processes such as grinding along clast boundaries are the dominant shaping mechanisms in the SDZ and CDZ foliated fault gouges. Time dependant chemical processes such as pressure dissolution and precipitation may be responsible for the some of the shaping processes of the survivor clasts in the SDZ and CDZ as described by *Bos and Spiers* [2001].

7. CONCLUSIONS

We have used XCT image analysis to better understand the characteristics of deformation with the gouge zones of the SAF at SAFOD. We have documented the shape-, orientation-, and size- distribution of survivor clasts to infer the kinematics and homogeneity of strain at the mesoscopic scale, and the processes of slip and flow of the gouge. We have also use the XCT imaging to determine the planar fabrics and infer kinematic relationships and relative timing of formation.

The observation that the size-, shape- and orientation-distributions of mesoscale, matrix-supported clasts are similar in the SDZ and CDZ gouge layers, and vary little with position in each gouge layer, is consistent with the hypothesis that aseismic creep in the SDZ and CDZ is achieved by distributed, shearing flow within the gouge layers.

The similarity of the shape and preferred orientations of large and small clasts, and the constant scaling relationship between frequency and size of clasts, suggests that comminution mechanisms are similar over the mm to m scale.

The consistency between the shape preferred orientation and simple-shear, strike-slip kinematics, and the marked difference of PSD, fabric, cohesion and clast lithology of the gouge with that of the adjacent rock, is consistent with the hypothesis that the vast majority of the shear displacement on the SAF at SAFOD is accommodated within the gouge layers and the gouge displays a mature, nearly steady-state structure.

The lenticular shapes of the clasts in the gouge, and the acute-angle, sharp-tipped edges of many clasts support the interpretation that reduction of clast size occurs by

mechanical and chemical surface-shaping processes rather than intraclast fracture or flow. The preservation of delicate edges of clasts implies that rotation of clasts occurs at low rates relative to those of surface-shaping processes.

The incohesive nature of the gouge matrix suggests microscopic fracture and interparticle sliding are the dominant microscale deformation processes, and the apparent stability of lenticular clasts aligned parallel to the gouge layer suggests contacts between matrix and clasts are best described as frictional slip surfaces.

REFERENCES

Almeida, R. (2007), Mesoscale fracture fabric and paleostress along the San Andreas Fault at SAFOD, M.S. thesis, Texas A&M University, College station, Texas.

An, Lin Ji and Sammis, C. G. (1994), Particle size distribution of cataclastic fault materials from southern California: A 3-D study, *Pure and Applied Geophysics, 143* (1-3), 203-227

Anderson, E. M. (1951), *The Dynamics of Faulting and Dyke Formation with Applications to Britain*, Oliver and Boyd, Edinburgh, Scotland, United Kingdom, 206 pp.

Ando, M. (2001), Geological and geophysical studies of the Nojima Fault from drilling: An outline of the Nojima Fault Zone Probe, *Isl. Arc., 10*(3-4), 206-214.

Atwater, Tanya, 1970, Implications of plate tectonics for the Cenozoic tectonic evolution of western North America. *Bull. Geol. Soc. Amer., 81*, 3513-3536.

Atwater, T., 1989, Plate tectonic history of the northeast Pacific and western North America, in Winterer, E. L., Hussong, D. M., and Decker, R. W., eds., The Eastern Pacific Ocean and Hawaii: Geological Society of America, Boulder, Colorado, The Geology of North America, pp 21-72.

Bell, T. H., and M. A. Etheridge (1973), Microstructure of mylonites and their descriptive terminology, *Lithos, 6*, 1973.

Boness, N. L., and M. D. Zoback (2004), Stress-induced seismic velocity anisotropy and physical properties in the SAFOD Pilot Hole in Parkfield, CA, *Geophysical Research Letters, 31*(15).

Bonnet, E., O. Bour, N. E. Odling, P. Davy, I. Main, P. Cowie, and B. Berkowitz (2001), Scaling of Fracture Systems in Geological Media, *Rev. Geophys., 39*(3), 347-383.

Borg, I., M. Friedman, J. Handin, and D. V. Higgs (1960), Experimental deformation of St. Peter Sand: a study of cataclastic flow, In: Rock Deformation (a symposium). *Geo. Soc. am. Mem., 79*, 133-191.

Bos, B., C. J. Peach, and C. J. Spiers (2000a), Slip behavior of simulated gouge-bearing faults under conditions favoring pressure solution, *Journal of Geophysical Research-Solid Earth, 105*(B7), 16699-16717.

Bos, B., C. J. Peach, and C. J. Spiers (2000b), Frictional-viscous flow of simulated fault gouge caused by the combined effects of phyllosilicates and pressure solution, *Tectonophysics, 327*(3-4), 173-194.

Bos, B., and C. J. Spiers (2001), Experimental investigation into the microstructural and mechanical evolution of phyllosilicate-bearing fault rock under conditions favouring pressure solution, *Journal of Structural Geology, 23*(8), 1187-1202.

Bos, B., and C. J. Spiers (2002), Frictional-viscous flow of phyllosilicate-bearing fault rock: Microphysical model and implications for crustal strength profiles, *Journal of Geophysical Research-Solid Earth, 107*(B2).

Brune, J. N., T. L. Henyey, and R. F. Roy (1969), Heat flow, stress, and rate of slip along San Andreas Fault, California, *Journal of Geophysical Research, 74*(15), 3821-3852.

Byerlee, J. (1978), Friction of rocks, Pure and Applied Geophysics, 116(4-5), 615-626.

Chester, F. M., M. Friedman, and J. M. Logan (1985), Foliated cataclasites, *Tectonophysics, 111*(1-2), 139-146.

Chester, F. M., and J. M. Logan (1986), Implications for mechanical-properties of brittle faults from observations of the Punchbowl Fault Zone, California, *Pure and Applied Geophysics, 124*(1-2), 79-106.

Chester, F. M., J. P. Evans, and R. L. Biegel (1993), Internal structure and weakening mechanisms of the San Andreas Fault, *Journal of Geophysical Research-Solid Earth, 98*(B1), 771-786.

Chester, F. M., and J. S. Chester (1998), Ultracataclasite structure and friction processes of the Punchbowl fault, San Andreas system, California, *Tectonophysics, 295*(1-2), 199-221.

Chester, F. M., and J. S. Chester (2010 Personal Communication).

Chester, J. S., F. M. Chester, and A. K. Kronenberg (2005), Fracture surface energy of the Punchbowl fault, San Andreas system, *Nature, 437*(7055), 133-136.

Chester, J. S., F. M. Chester, D. Kirschner, R. Almeida, J. P. Evans, R. N. Guillemette, S. Hickman, M. Zoback, and W. Ellsworth (2007), Deformation of sedimentary rock across the San Andreas Fault Zone: Mesoscale and microscale structures displayed in core frome SAFOD, *Eos Trans. AGU, 88*(52), Fall Meet . Supple., Absract T42C-05.

Chester, J. S., F. M. Chester, D. Kirschner, J. P. Evans, D. W. Sills, and C. G. Coble (2008), Structure of the San Andreas Fault Zone at SAFOD, Geological Society of America Annual Meeting, Houston, Texas. Abstracts with Programs.

Cladouhos, T. T. (1999a), Shape preferred orientations of survivor grains in fault gouge, *Journal of Structural Geology, 21*(4), 419-436.

Cladouhos, T. T. (1999b), A kinematic model for deformation within brittle shear zones, *Journal of Structural Geology, 21*(4), 437-448.

Coble, R. L. (1963), A model for boundary diffusion controlled creep in polycrystalline materials, *Journal of Applied Physics, 34*, 1679-1682.

Collettini, C., A. Niemeijer, C. Viti, and C. Marone (2009), Fault zone fabric and fault weakness, *Nature, 462*(7275), 907-U998.

Faulkner, D. R., A. C. Lewis, and E. H. Rutter (2003), On the internal structure and mechanics of large strike-slip fault zones: field observations of the Carboneras fault in southeastem Spain, *Tectonophysics, 367*(3-4), 235-251.

Flinn, D. (1962), On Folding during three dimensional progressive deformation, *Q. J. Geol. Soc. Lond., 118*(385-428).

Ghosh, S. K., and H. Ramberg (1976), Reorientation of inclusions by combination of pure shear and simple shear, *Tectonophysics, 34*, 1-70.

Hayman, N. W., B. A. Housen, T. T. Cladouhos, and K. Livi (2004), Magnetic and clast fabrics as measurements of grain-scale processes within the Death Valley shallow crustal detachment faults, *Journal of Geophysical Research-Solid Earth, 109*(B5), 16.

Hickman, S., and M. Zoback (2004), Stress orientations and magnitudes in the SAFOD pilot hole, *Geophysical Research Letters, 31*(15).

Hickman, S., M. Zoback, and W. Ellsworth (2004), Introduction to special section: Preparing for the San Andreas Fault Observatory at Depth, *Geophysical Research Letters, 31*(12).

Hirono, T., M. Sakaguchi, K. Otsuki, H. Sone, K. Fujimoto, T. Mishima, W. Lin, W. Tanikawa, M. Tanimizu, W. Soh, E. C. Yeh, and S. R. Song (2008), Characterization of slip zone associated with the 1999 Taiwan Chi-Chi earthquake: X-ray CT image analyses and microstructural observations of the Taiwan Chelungpu fault, *Tectonophysics, 449*(1-4), 63-84.

Huddlestone-Holmes, C.R. and Ketcham, R.A. (2010), An X-ray computed tomography study of inclusion trail orientations in multiple porphyroblasts from a single sample, *Tectonophysics, 480*(1-4), 305-320.

Isaacs, A. J., J. P. Evans, P. T. Kolesar, and T. Nohara (2008), Composition, microstructures, and petrophysics of the Mozumi fault, Japan: In situ analyses of fault zone properties and structure in sedimentary rocks from shallow crustal levels, *Journal of Geophysical Research-Solid Earth, 113*(B12), 17.

Jefferies, S. P., R. E. Holdsworth, T. Shimamoto, H. Takagi, G. E. Lloyd, and C. J. Spiers (2006a), Origin and mechanical significance of foliated cataclastic rocks in the cores of crustal-scale faults: Examples from the Median Tectonic Line, Japan, *Journal of Geophysical Research-Solid Earth, 111*(B12).

Jefferies, S. P., R. E. Holdsworth, C. A. J. Wibberley, T. Shimamoto, C. J. Spiers, A. R. Niemeijer, and G. E. Lloyd (2006b), The nature and importance of phyllonite

development in crustal-scale fault cores: an example from the Median Tectonic Line, Japan, *Journal of Structural Geology, 28*(2), 220-235.

Kanamori, H. (1994), Mechanics of earthquakes, *Annual Revision in Earth and Planetary Sciences, 22*, 207-237.

Keller, J. V. A., S. H. Hall, C. J. Dart, and K. R. McClay (1995), The geometry and evolution of a transpressional strike-slip system - the Carboneras Fault, Spain, *Journal of the Geological Society, 152*, 339-351.

Ketcham, R. A., and W. D. Carlson (2001), Acquisition, optimization and interpretation of X-ray computed tomographic imagery: applications to the geosciences, *Comput. Geosci., 27*(4), 381-400.

Ketcham, R. A. (2005), Computational methods for quantitative analysis of three-dimensional features in geological specimens, *Geosphere, 1*(1), 32-41.

Kim, T. H., E. Putra, and D. S. Schechter (2006), Analyzing tensleep natural fracture properties using X-ray CT scanning, *e-Journal of Reservoir Engineering*, PJO(1), 1.

Kitajima, K., J. S. Chester, F. M. Chester, and T. Shimamoto (2010), High-speed friction of Punchbowl Fault ultracataclasite in rotary shear: Characterization of fricitonal heating, mechanical behavior, and microstructure evolution, Journal of Geophysical *Research in press*.

Lachenbruch, A. H., and J. H. Sass (1980), Heat-flow and energetics of the San Andreas Fault Zone, *Journal of Geophysical Research, 85*(NB11), 6185-6222.

Lachenbruch, A. H., and J. H. Sass (1992), Heat-flow from Cajon Pass, fault strength, and tectonic implications, *Journal of Geophysical Research-Solid Earth, 97*(B4), 4995-5015.

Lee, H. K., and H. S. Kim (2005), Comparison of structural features of the fault zone developed at different protoliths: crystalline rocks and mudrocks, *Journal of Structural Geology, 27*(11), 2099-2112.

Larouziere, F. D. d., J. Bolze, P. Bordet, J. Hernandez, C. Montenat, and P. Ott D'Estevou (1988), The Betic segment of the lothospheric Trans-Alboran shear zone during the late Miocene, *Tectonophysics, 152*, 41-52.

Lister, G. S., and A. W. Snoke (1984), S-C mylonites, *Journal of Structural Geology, 6,* 617-638.

Mair, K., and C. Marone (1999), Friction of simulated fault gouge for a wide range of velocities and normal stresses, *Journal of Geophysical Research-Solid Earth, 104*(B12), 28899-28914.

March, A. (1932), Mathematische theorie der regelung nach der korngestalt bei affiner deformation, *Zeitschrift fur Kristallographie, 81*, 285-297.

Mizoguchi, K., T. Hirose, T. Shimamoto, and E. Fukuyama (2009), High-velocity frictional behavior and microstructure evolution of fault gouge obtained from Nojima fault, southwest Japan, *Tectonophysics, 471*(3-4), 285-296.

Moore, D. E., and M. J. Rymer (2007), Talc-bearing serpentinite and the creeping section of the San Andreas fault, *Nature, 448*(7155), 795-797.

Mount, V. S., and J. Suppe (1987), State of stress near the San Andreas Fault - Implications for wrench tectonics, *Geology, 15*(12), 1143-1146.

Novelline, Robert A. (2004), Basic Concepts, in *Squire's Fundamentals of Radiology*, Harvard University Press, 6th edition, p. 7.

Pennacchioni, G., G. Di Toro, and N. S. Mancktelow (2001), Strain-insensitive preferred orientation of porphyroclasts in Mont Mary mylonites, *Journal of Structural Geology, 23*(8), 1281-1298.

Reinen, L. A. (2000), Seismic and aseismic slip indicators in serpentinite gouge, *Geology, 28*(2), 135-138.

Rice, J. R. (1983), Constitutive relations for fault slip and earthquake instabilities, *Pure and Applied Geophysics, 121*(3), 443-475.

Rutter, E. H., R. H. Maddock, S. H. Hall, and S. H. White (1986), Comparative microstructures of natural and experimentally produced clay-bearing fault gouges, *Pure and Applied Geophysics, 124*(1-2), 3-30.

Sammis, C., G. King, and R. Biegel (1987), The kinematics of gouge deformation, *Pure and Applied Geophysics, 125*(5), 777-812.

Schleicher, A. M., S. N. Tourscher, B. A. van der Pluijm, and L. N. Warr (2009a), Constraints on mineralization, fluid-rock interaction, and mass transfer during faulting at 2-3 km depth from the SAFOD drill hole, *Journal of Geophysical Research-Solid Earth, 114*.

Schleicher, A. M., L. N. Warr, and B. A. V. van der Pluijm (2009b), On the origin of mixed-layered clay minerals from the San Andreas Fault at 2.5-3 km vertical depth

(SAFOD drillhole at Parkfield, California), *Contributions to Mineralogy and Petrology, 157*(2), 173-187.

Sibson, R. H. (1977), Fault Rocks and fault mechanisms, *Journal of the Geological Society of London, 133*(Part 3):191-213.

Sibson, R. H. (1986), Brecciation processes in fault zones - Inferences from earthquake rupturing, *Pure and Applied Geophysics, 124*(1-2), 159-175.

Sieh, K. E. (1978), Slip along San Andreas Fault associated with great 1857 earthquake, *Bulletin of the Seismological Society of America, 68*(5), 1421-&.

Sleep, N. H., and M. L. Blanpied (1992), Creep, compaction and the weak rheology of major faults, *Nature, 359*(6397), 687-692.

Solum, J. G., and B. A. van der Pluijm (2004), Phyllosilicate mineral assemblages of the SAFOD Pilot Hole and comparison with an exhumed segment of the San Andreas Fault System, *Geophysical Research Letters, 31*(15).

Solum, J. G., S. H. Hickman, D. A. Lockner, D. E. Moore, B. A. van der Pluijm, A. M. Schleicher, and J. P. Evans (2006), Mineralogical characterization of protolith and fault rocks from the SAFOD Main Hole, *Geophysical Research Letters, 33*(21).

Tanaka, H., C. Y. Wang, W. M. Chen, A. Sakaguchi, K. Ujiie, H. Ito, and M. Ando (2002), Initial science report of shallow drilling penetrating into the Chelungpu fault zone, Taiwan, *Terr. Atmos. Ocean. Sci., 13*(3), 227-251.

Thurber, C., S. Roecker, H. Zhang, S. Baher, and W. Ellsworth (2004), Fine-scale structure of the San Andreas fault zone and location of the SAFOD target earthquakes, *Geophysical Research Letters, 31*(12).

Titus, S. J., C. DeMets, and B. Tikoff (2006), Thirty-five-year creep rates for the creeping segment of the San Andreas fault and the effects of the 2004 Parkfield earthquake: Constraints from alignment arrays, continuous global positioning system, and creepmeters, *Bulletin of the Seismological Society of America, 96*(4), S250-S268.

White, S. (1976), The effects of strain on the microstructure, fabrics, and deformation mechanisms in quartzite, Philos. Trans. R. Soc. London, Ser. A, 283, 69-86.

Williams, C. F., F. V. Grubb, and S. P. Galanis (2004), Heat flow in the SAFOD pilot hole and implications for the strength of the San Andreas Fault, *Geophysical Research Letters, 31*(15).

Wilson, J. E., J. S. Chester, and F. M. Chester (2003), Microfracture analysis of fault growth and wear processes, Punchbowl Fault, San Andreas System, California, *Journal of Structural Geology, 25*(11), 1855-1873.

Zoback, M., S. Hickman, and W. Ellsworth (in press), Scientific drilling into the San Andreas Fault Zone, *Eos: Transactions of the Geophysical Union*.

Zoback, M. D., and J. H. Healy (1992), Insitu stress measurements to 3.5 km depth in the Cajon Pass scientific-research borehole - Implications for the mechanics of crustal faulting, *Journal of Geophysical Research-Solid Earth, 97*(B4), 5039-5057.

APPENDIX

FIGURES AND TABLES

Figure 1. Map of California showing the location of SAFOD, the creeping section (green), and locked sections of the San Andreas Fault (red) [modified from Hickman et al., 2004].

[modified from *Hickman et al.*, 2004]

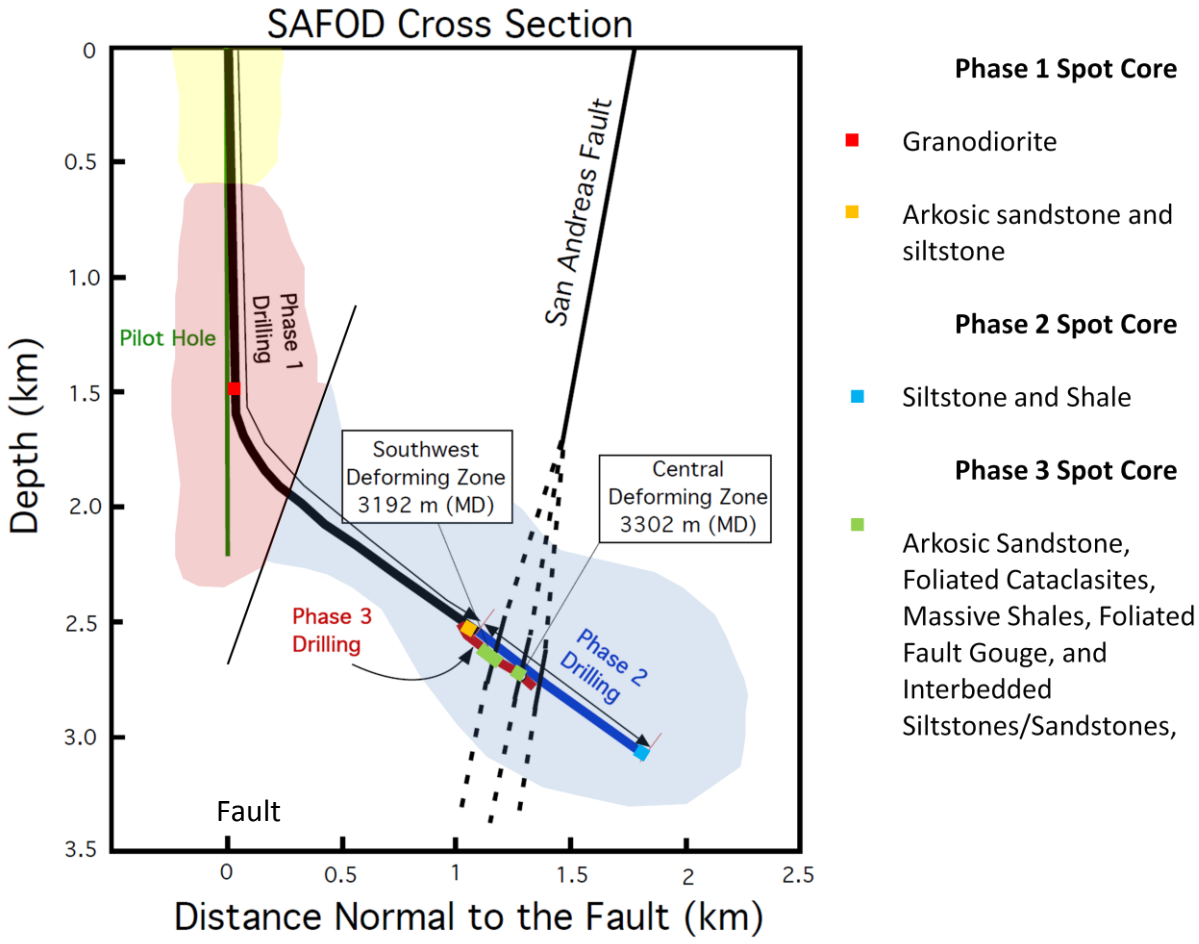

Figure 2. A cross section diagram of the SAFOD drilling phases. Pilot hole (green), phase 1 (black), phase 2 (blue), and phase 3 (red). All core taken from phase 3 were XCT scanned at the Texas A&M Petroleum Engineering Imaging Laboratory. The focus of our research was the Southwest Deforming Zone (SDZ) at 3192 m (MD) and the Central Deforming Zone (CDZ) at 3302 m (MD). The high resolution scans used core from the CDZ [modified from Chester et al., 2008].

[modified from *Chester et al.*, 200]

Table 1. Core interval and depth extent of lithologic units in Phase 3 core samples

Depth Interval m (MD)		Coring interval		*Lithology
3143.5	3146.6	HECR1S1	HECR1S4	Greenish Gray Pebbly Sandstone
3146.6	3147.9	HECR1S4	HECR1S5	Dark Grayish-Black Siltstone
3147.9	3154.7	HECR1S5	HECR2S6	Grayish-Red Pebbly Sandstone
3188.8	3196.0	HGCR1S1	HGCR2S4	Foliated Siltstone-Shale Cataclasite
3196.0	3198.5	HGCR2S4	HGCR2S6	Massive, Grayish-Black Shale
3198.5	3200.2	HGCR2S7	HGCR2S9	Foliated Fault Gouge
3200.5	3201.6	HGCR3S1	HGCR3S2	Sheared Siltstone and Shale
3297.1	3298.7	HGCR4S1	HGCR4S2	Sheared Siltstone Sandstone
3298.7	3301.3	HGCR4S2	HGCR4S5	Foliated Fault Gouge
3301.3	3303.7	HGCR4S5	HGCR5S2	Sheared Siltstone and Mudstone
3303.7	3305.5	HGCR5S2	HGCR5S4	Massive Siltstone and Very Fine Sandstone
3305.5	3307.6	HGCR5S4	HGCR5S6	Sheared and Fractured Siltstone to Very Fine Sandstone
3309.6	3313.2	HGCR6S1	HGCR6S5	Sheared and Fractured Claystone, Mudstone, and Siltstone
3313.2	3314.0	HGCR6S5	HGCR6S6	Sheared Claystone and Shale

*From SAFOD Phase 3 core atlas

Table 2. Rotation angles relative to the black reference line (BRL) to align core sections and orient course to the geographic reference frame.

		XCT Scan		Contigous Sections	Interval Alignment	Summary Rotation	Summary Geographic	Borehole Survey	
Core Number	**Lithology**	**Final Angle from A to BRL**	**Depth (MD) Meters**	**Angle from BRL of Individual Section to BRL of Reference Core for Contiguous Section**	**Angle from BRL of Reference Core for Contigous Section To BRL of Interval Referenc Core**	**Angle from BRL of Interval Refence Core to BRL of Individual Section**	**Angle from Top of Borehole to BRL of Individual Section**	**Borehole Orientation**	**Data used for the borehole rotation**
HGCR1S1	Foliated Siltstone-Shale Cataclasite	4.8	3186.71-3187.5	207	150.3	3	-66	39, 040.8	150.3 based on aligning foliated cataclasite in base of HGCR1S5 foliated cataclasite in top of HGCR2S1
HGCR1S2	Foliated Siltstone-Shale Cataclasite	-5.4	3187.5-3188.3	0	150.3	-150	141	39, 040.8	"
HGCR1S3	Foliated Siltstone-Shale Cataclasite	-43.5	3188.3-3189.3	0	150.3	-150	141	39, 040.8	"
HGCR1S4	Foliated Siltstone-Shale Cataclasite	-18.5	3189.3-3190.2	0	150.3	-150	141	39, 040.8	"
HGCR1S5	Foliated Siltstone-Shale Cataclasite	0	3190.2-3190.7	Reference core	150.3	-150	141	39, 040.8	"
HGCR2S1	Foliated Siltstone-Shale Cataclasite	0	3191-3191.8	85.2	0	0	-69	39, 040.8	(-69) based on alignig foliated cataclasite in base of HGCR2S6 through the top of HGCR2S7 to GVR layering 10447-10480 ft MD
HGCR2S2	Foliated Siltstone-Shale Cataclasite	0	3191.8-3192.7	85.2	0	0	-69	39, 040.8	"
HGCR2S3	Foliated Siltstone-Shale Cataclasite	-60.3	3192.7-3193.6	85.2	0	0	-69	39, 040.8	"
HGCR2S4	Foliated Siltstone-Shale Cataclasite/Massive, Grayish-Black Shale	0	3193.6-3194.4	0	0	0	-69	39, 040.8	"
HGCR2S5	Massive, Grayish-Black Shale	0	3134.4-3195.3	0	0	0	-69	39, 040.8	"
HGCR2S6	Massive, Grayish-Black Shale	0	3195.3-3196.2	0	0	0	-69	39, 040.8	"
HGCR2S7	Foliated Fault Gouge	0	3196.2-3197.2	Reference core	0	0	-69	39, 040.8	"
HGCR2S8 Half 1	Foliated Fault Gouge	NA	3197.2-3197.7	45	na	-45	-114	39, 040.8	"
HGCR2S8 Half 2	Foliated Fault Gouge	NA	3197.2-3197.7	185+45	na	-230	61	39, 040.8	"
HGCR3S1	Sheared Siltstone Mudstone	0	3198.4-3199	0 for slices 414-610	0	0	134	39, 040.8	134 based on STAR bedding over 10480-10492 ft MD
HGCR3S2	Sheared Siltstone Mudstone	0	3199-3199.5	Reference core	0	0	134	39, 040.8	"
HGCR4S2	Sheared Siltstone and Sandstone/Foliated Fault Gouge	-1.2	3295.8-3296.6	0	0	0	-95	29.5, 033.2	based off kinematic comparison to clast orientation distribution in SWCZ and Brigham major axes dipping 0 degrees
HGCR4S3	Foliated Fault Gouge	-10.7	3296.6-3297.5	Reference Core	0	0	-95	29.5, 033.2	"
HGCR4S4	Foliated Fault Gouge	0.9	3297.5-3298.4	176.45	0	-176.45	88.9	29.5, 033.2	"
HGCR4S5	Foliated Fault Gouge/Sheared Siltstone Mudstone	-9.4	3298.4-3299.3	0	0	0	-95	29.5, 033.2	"

[J.S. Chester and F.M. Chester 2010]

a.

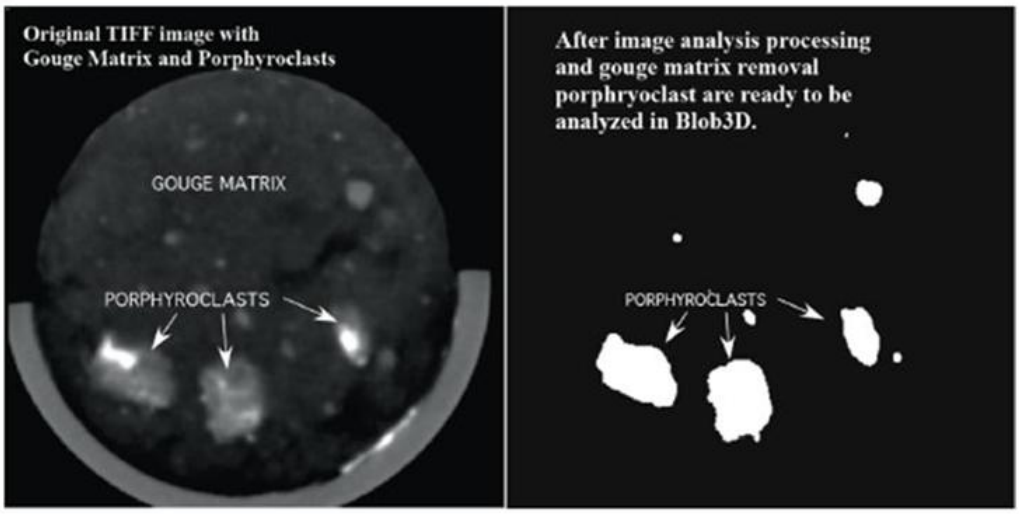

b.

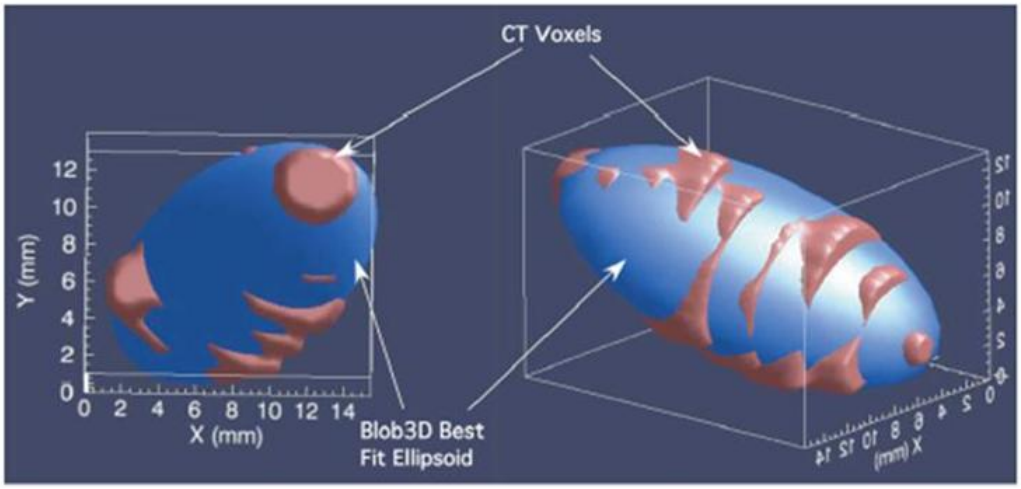

Figure 3. Image analysis techniques used for gathering survivor clast data. ImageJ is used separate the clasts from the gouge matrix. Separation is accomplished by converting the original grayscale images to binary images where only the survivor clasts are visible. The binary images are imported into Blob3D for shape, size, and spatial analysis. (a.) Before and after threshold processing to separate survivor clasts from the gouge matrix. Survivor clasts have a higher grayscale value than the gouge matrix. After threshold processing only the survivor clasts remain in white. (b.) Blob3D renderings. Brown are "Blobs" and blue is the best fit ellipsoid.

a.

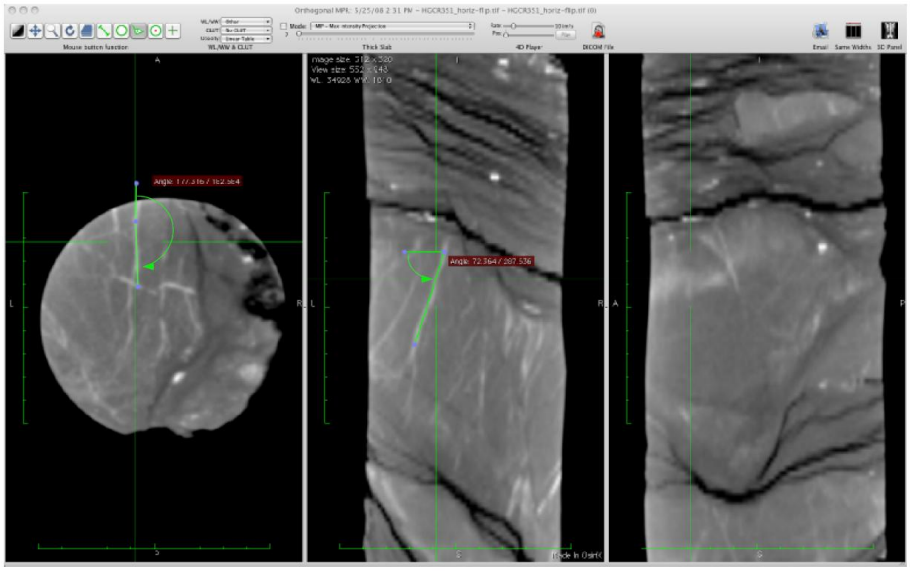

b.

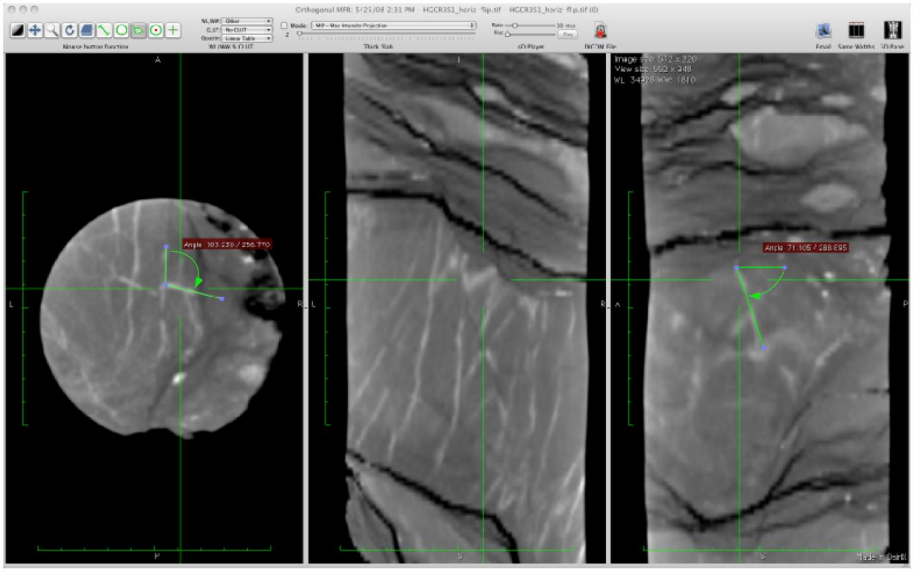

Figure 4. Planar fabric measuring (in OsiriX) technique for measuring planar fabric elements. (a.) Technique for measuring planar fabric elements which are oriented from 315° to 45° and from 135° to 225° in the slice views. (b.) Technique for measuring planar fabric elements which are oriented from 45° to 135° and from 225° to 315° in the slice views.

Table 3. Observed range of radiodensity of fabric elements in CT images.

Lithology	Fabric Element	Radiodensity Low Resolution	Radiodensity High Resolution
Open fractures	fractures	(-1000) to (-900)	NA
Foliated fault gouge	gouge matrix	1400-1500	22000-23000
Foliated fault gouge	survivor clasts	1600-2100	24000-25000
Foliated cataclasite	cataclasite matrix	1400-1500	NA
Foliated cataclasite	cataclasite foliations	3000-3200	NA
Foliated cataclasite	survivor clasts	4000-4200	NA
Massive shale	shale matrix	1500-1600	NA
Massive shale	veins	1700-1800	NA
Interbedded sandstone and siltstones	shale matrix	1700-1800	NA
Interbedded sandstone and siltstones	siltstone and sandstone matrix	2000-2100	NA
Interbedded sandstone and siltstones	veins	2400-2500	NA

a.

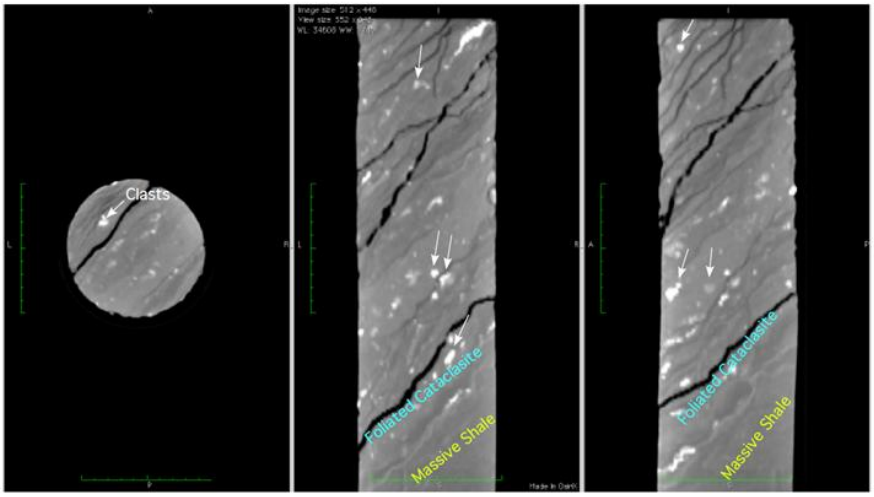

b.

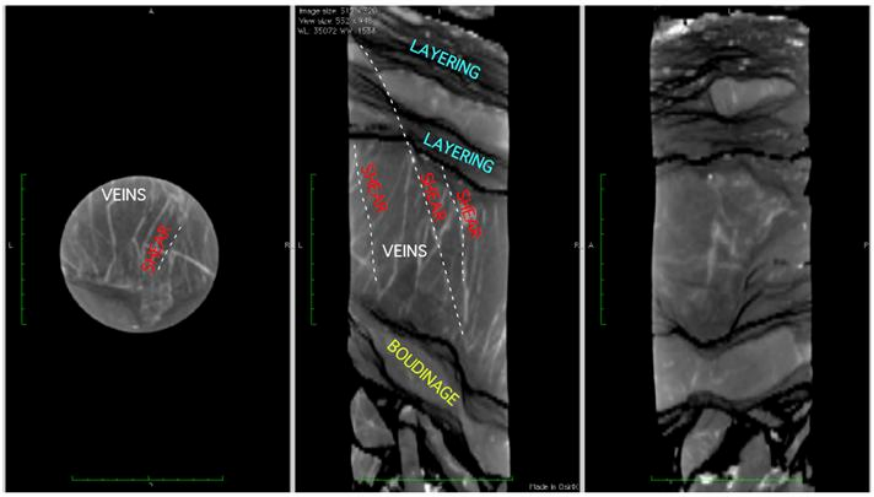

Figure 5. Osirix screenshot of the foliated cataclasite interval west of the SDZ gouge and the interbedded siltstone/sandstones interval to the east of the SDZ gouge. (a) Foliated cataclasites west of the SDZ. Noted are clasts, the foliation, and the sharp boundary of the massive shale interval. (b) Sheared interbedded siltstone/sandstone interval. Structures labeled are veins (white), shears (red), layering (sky blue), and boudinage (yellow).

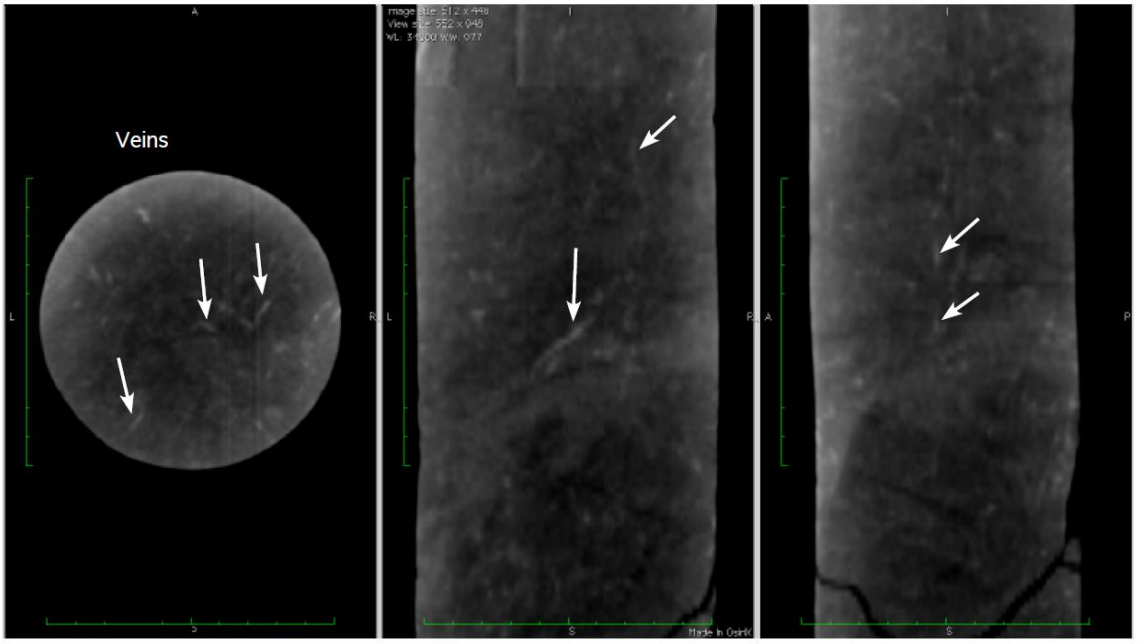

Figure 6. Osirix screenshot of veins within the massive shale interval. The veins are small and appear within the slice view and two slab views.

a.

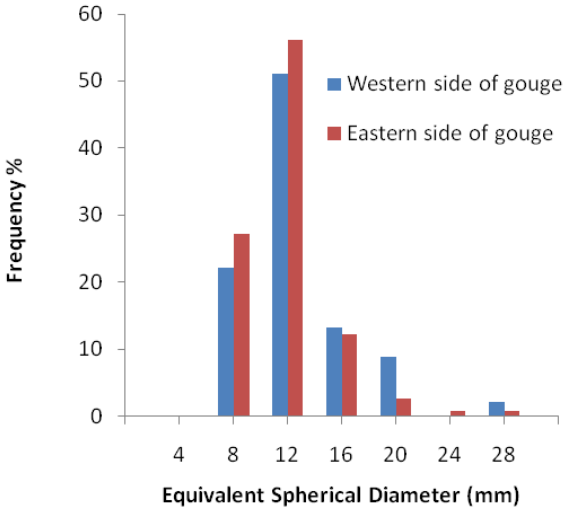

b.

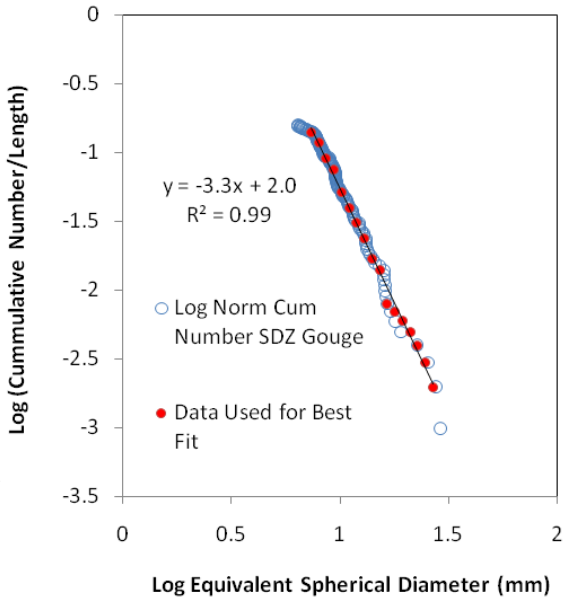

Figure 7. . Histogram of equivalent spherical diameters for the survivor clasts from SDZ western and eastern gouges, and the combined particle size distribution for the survivor clasts from SDZ western and eastern gouges. (a.) Equivalent spherical diameter (mm) histogram. Western (Blue) and eastern (Red) gouges (b.) Combined particle size distribution (PSD) for clasts within the western and eastern SDZ gouge from computed tomography imaging and particle analysis using Blob3D from the low resolution dataset. Open blue circles represent all clasts images. Red closed circles represent data used for the best power law trendline. Clast sizes from log equivalent spherical diameter 0.81 mm to 1.46 mm were imaged using the low resolution scanner. The number of clasts are normalized by the volume of core scanned (8,204,607 mm^3).

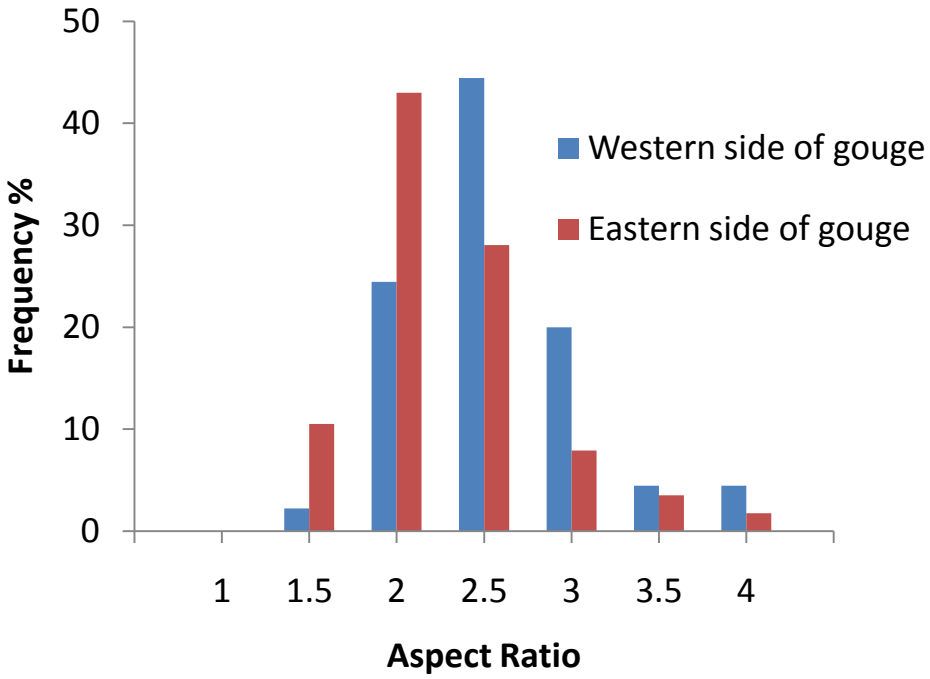

Figure 8. Histogram of axial ratios for the survivor clasts from SDZ western (Blue) and eastern (Red) gouges.

a.

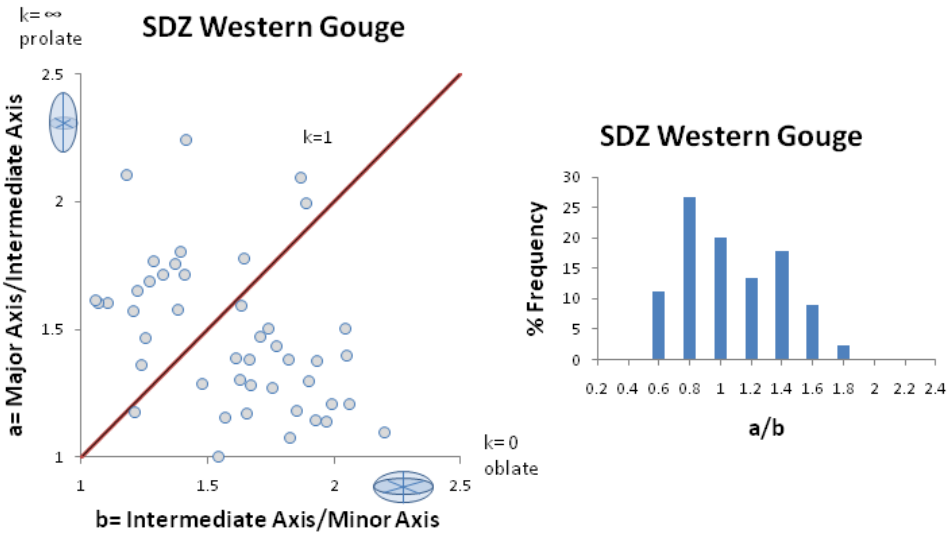

b.

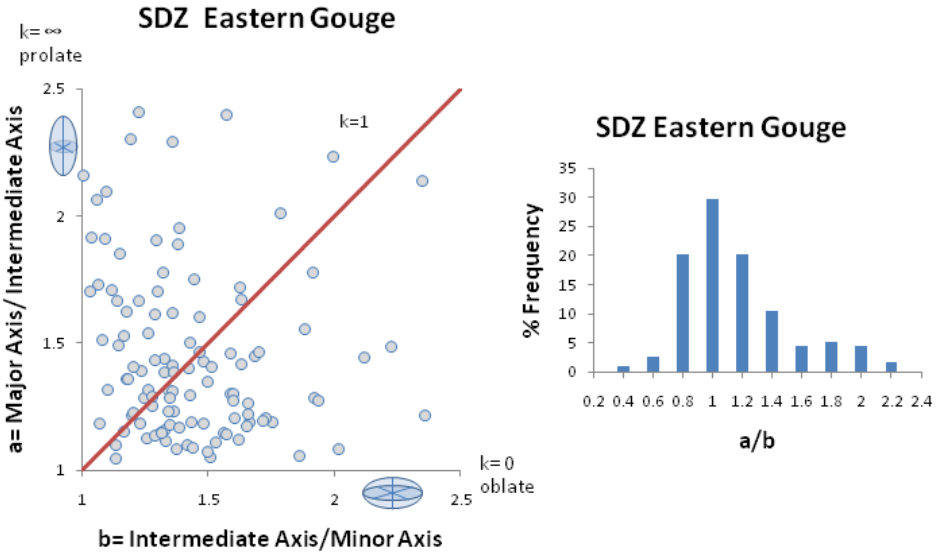

Figure 9. Flinn diagrams of ellipsoidal shaped survivor clasts from the SDZ western and eastern gouge zones. In the diagram, K = ∞ (Y axis) describes prolate uniaxial ellipsoids, values from 1< k <∞ describe prolate triaxial ellipsoids, k = 1 describes scalene ellipsoids, 0 < k <1 describes oblate triaxial ellipsoids, and k = 0 (X axis) describes all oblate uniaxial ellipsoids [*Flinn*, 1962]. The percent frequency histograms represent the statistical shape distribution in the Flinn diagrams. (a)Western gouge Flinn diagram with histogram. (b) Eastern gouge Flinn diagram with histogram.

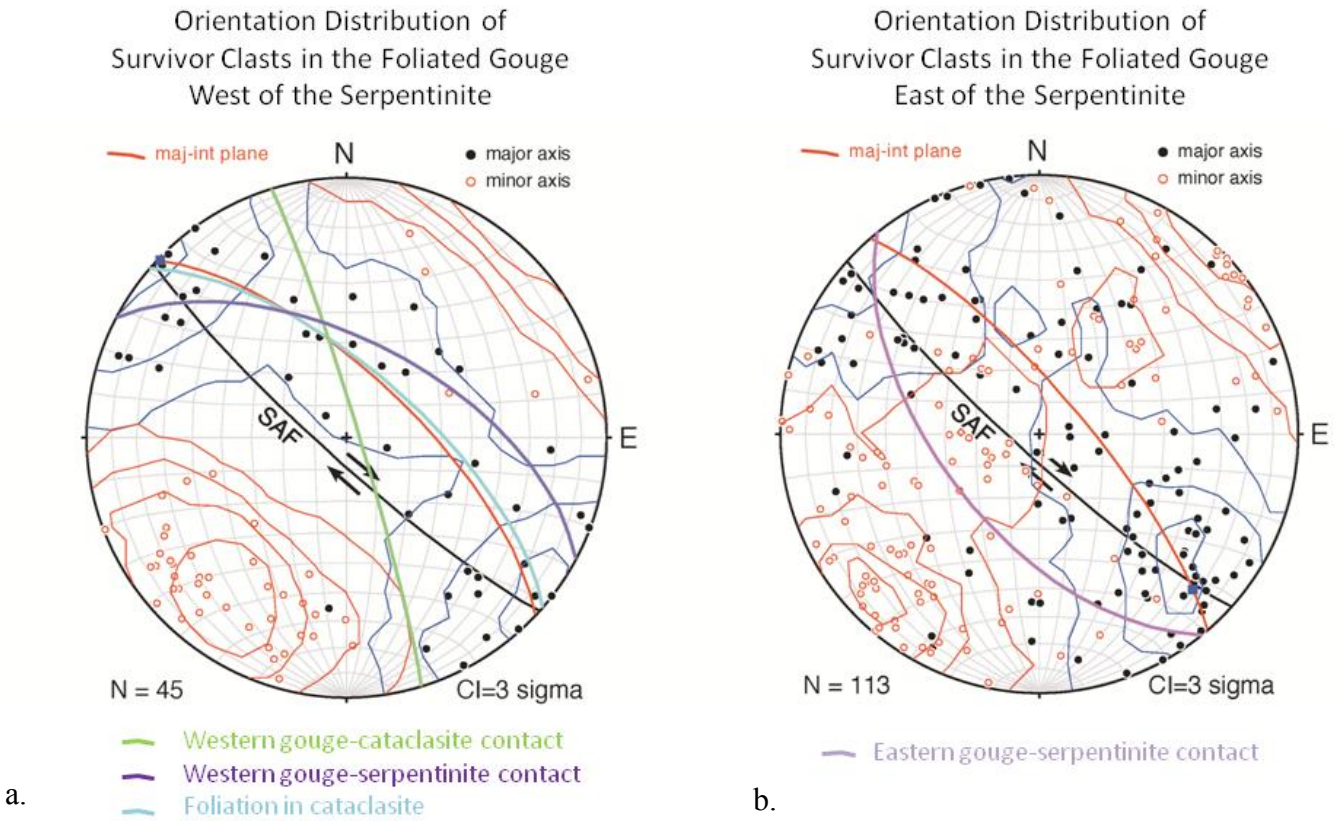

Figure 10. Orientation distribution of survivor clasts from the SDZ gouge as a function of location The orientation distributions are plotted in lower hemisphere equal area projections. The poles of the major and minor axes of survivor clasts are rotated into geographic orientation using fabric data from phase 2 image logs. Contoured using Kamb method with three sigma contour interval. (a.) Clasts from the gouge west of the serpentinite block plotted with western gouge-cataclasite contact, western gouge-serpentinite contact, and foliation in cataclasite. (b) Clasts from the gouge east of the serpentinite block plotted with lower gouge-serpentinite contact.

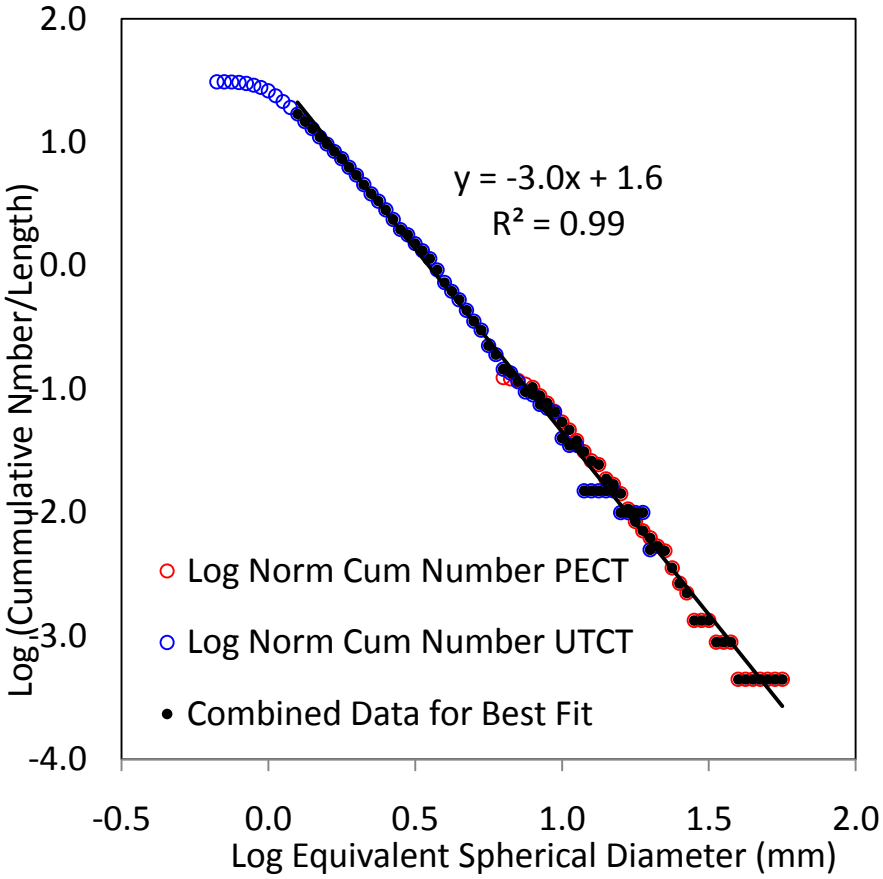

Figure 11. Particle size distribution for clasts within CDZ based on low and high resolution X-ray computed tomography imaging and particle analysis using Blob3D [*Ketcham*, 2005]. Open blue circles represent all clasts image. Red closed circles represent data used for the best power law trendline. Clast sizes from 1.77 mm to 0.80 mm were imaged using the low resolution dataset and from 1.30 mm to 0.10 mm using the high resolution dataset. Low-resolution images define clasts that have a minimum axis dimension of 5 mm or more, and that are completely contained within the 101.6 mm diameter core. High-resolution images define clasts that have a minimum axis dimension of .65 mm or more. The number of clasts are normalized by the volume of core scanned (1,621,463 mm for high resolution data and 18,225,254 mm^3 for the low resolution data).

a.

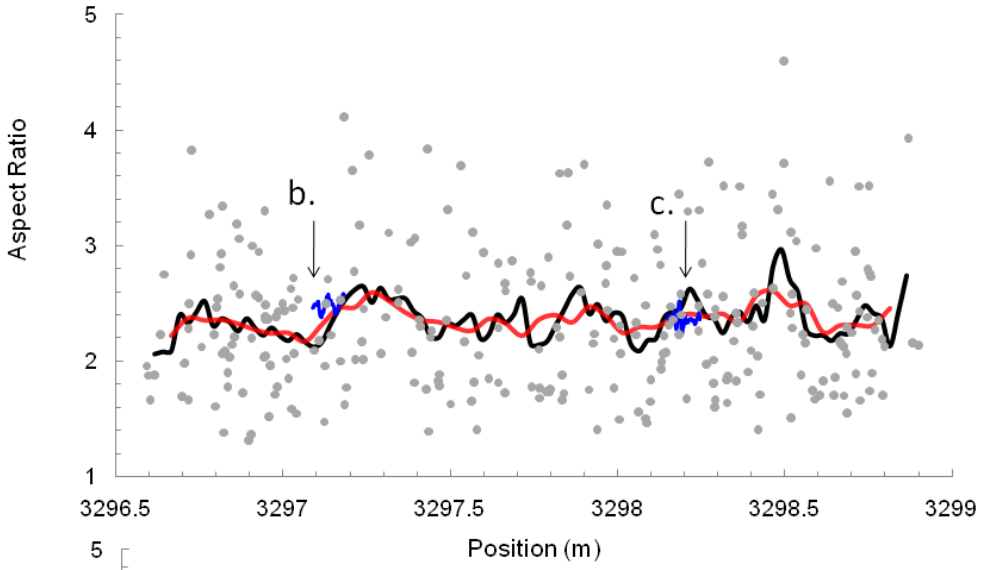
Aspect Ratio
5
4
3
2
1
b.
c.
3296.5
3297
3297.5
3298
3298.5
3299
Position (m)

b.

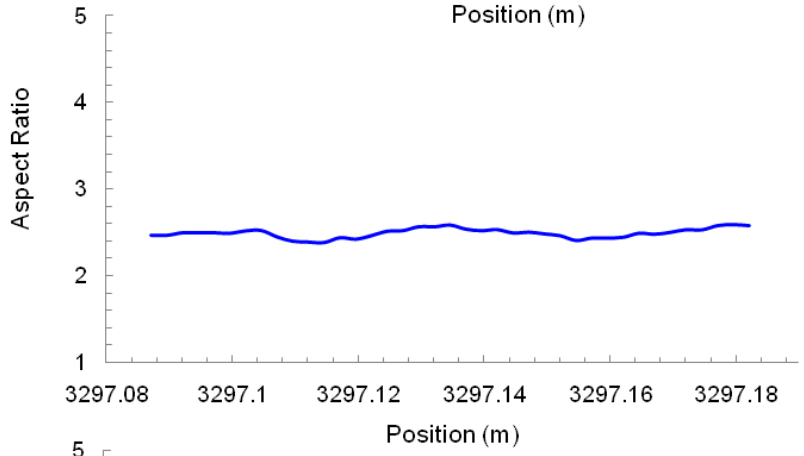
Aspect Ratio
5
4
3
2
1
3297.08
3297.1
3297.12
3297.14
3297.16
3297.18
Position (m)

c.

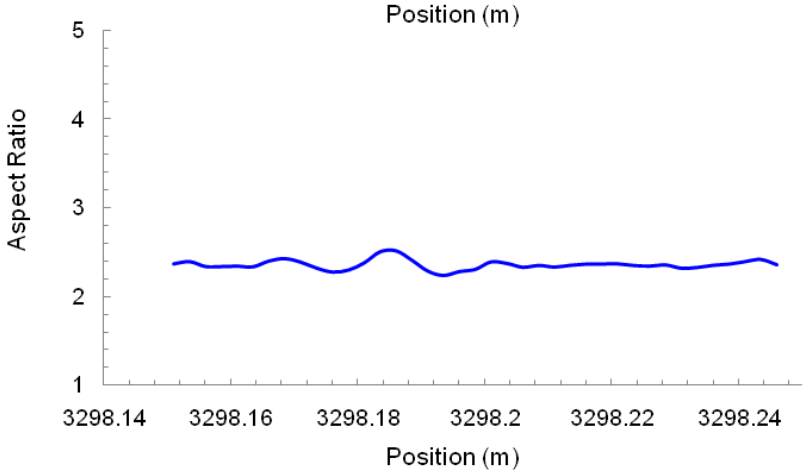
Aspect Ratio
5
4
3
2
1
3298.14
3298.16
3298.18
3298.2
3298.22
3298.24
Position (m)

d.

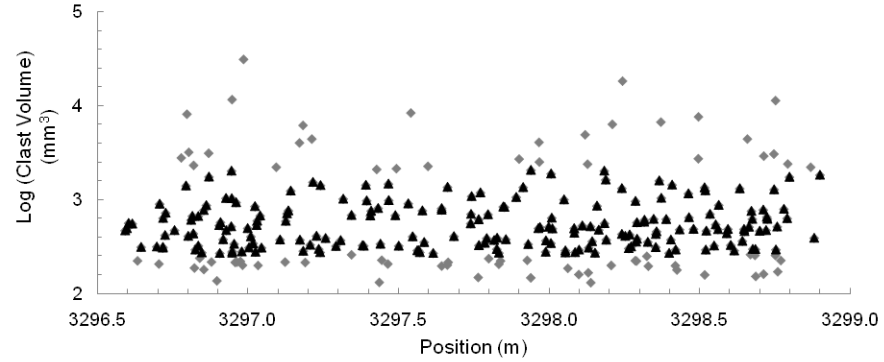

e.

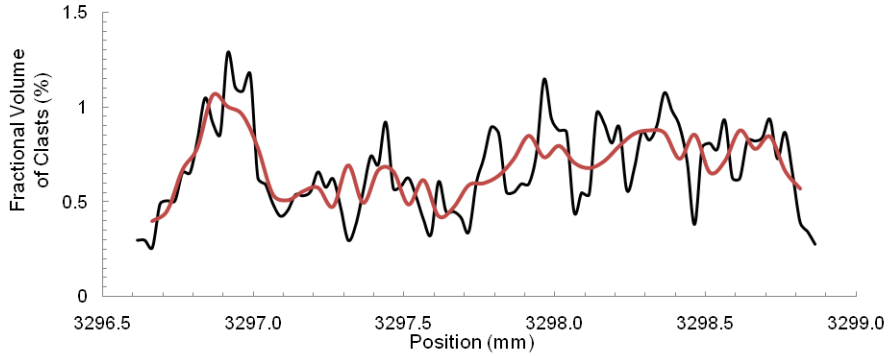

Figure 12. The variation in the abundance and shape of survivor-clasts across the main gouge zone. Analysis of clasts within the main gouge zone as a function of position (calculate the measured depth). (a.) Simple running average of clast aspect ratio as a function of position. Clasts considered are those that were imaged using the low resolution scanner, that have a minimum axis dimension of 5 mm or more, and that are completely contained within the 101.6 mm diameter core. Solid curves represent the running average aspect ratios for clasts having centroid points that fall within 100 mm (black curve) and 200 mm (red curve) intervals, calculated for 25 and 50 mm steps in position, respectively. (b.) Running average aspect ratio of clasts having centroid points that fall within 10 mm intervals, calculated for 2.5 mm steps from higher resolution scans over the 3297.1-3297.2 m MD interval (c.) Running average aspect ratio of clasts having centroid points that fall within 10 mm intervals, calculated for 2.5 mm steps from high resolutions scans over the 3298.1-3298.2 m (MD) m interval. (d.) Log (clast volume) as a function of position for all clasts that are completely contained within the 101.6 mm diameter core. Gray diamonds represent all clasts imaged using the low resolution scanner that have a minimum axis dimension of 5 mm or more. Black triangles represent the subset of clasts having a Log (Equivalent Spherical Diameter) of 0.9 to 1.2. (e.) Running fractional volume for the subset of clasts having a Log (equivalent spherical diameter) of 0.9 to 1.2, shown above. Running fractional volume is the volume of clasts that are completely contained within a 200 mm interval of core, normalized by the interval volume and calculated for 50 mm steps in position.

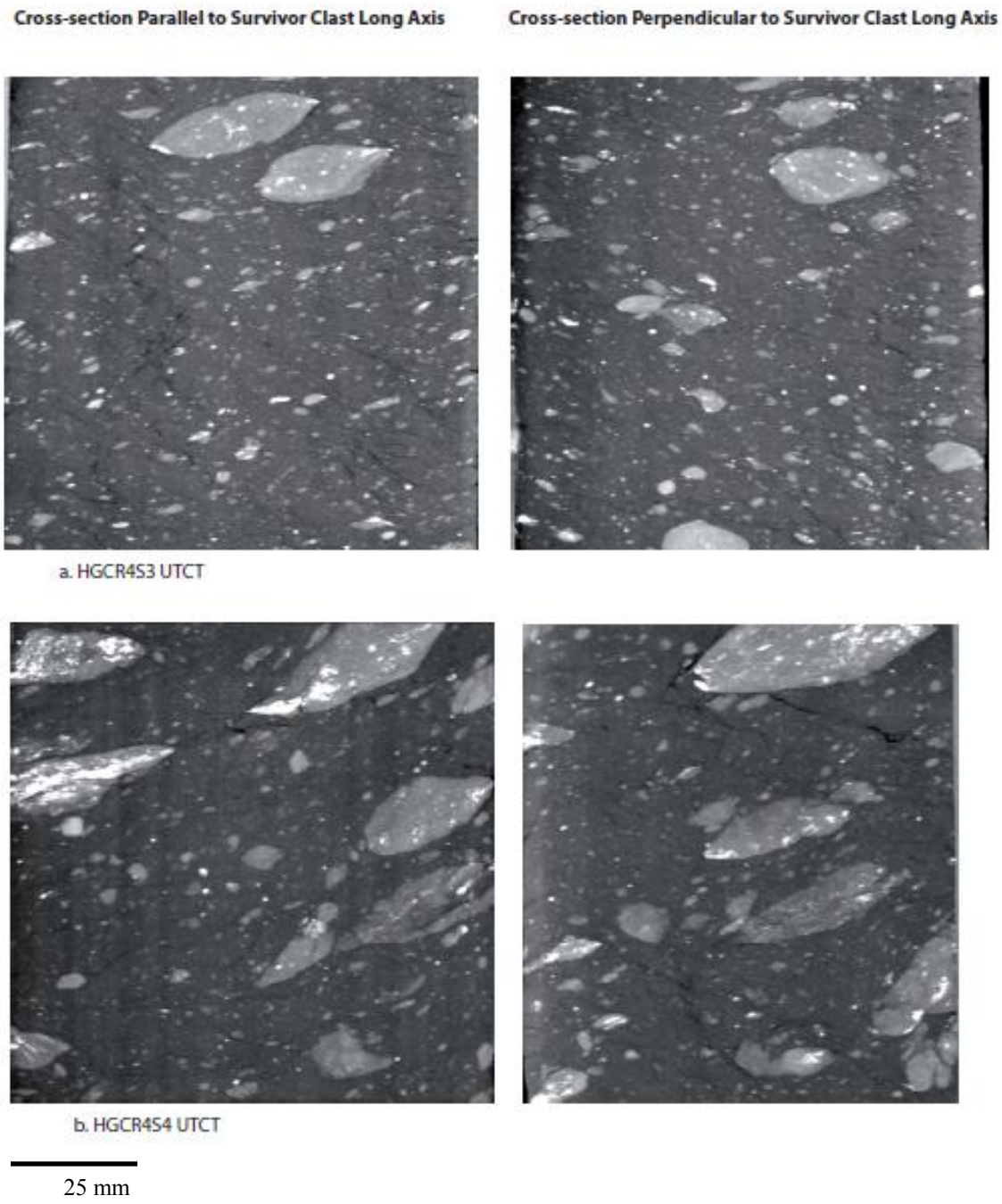

Figure 13. High resolution thickslab Osirix cross-sectional slices parallel to the survivor clast long axis and perpendicular to the survivor clast long axis. The thickslab Osirix cross-sectional slice reveal fine clast tips of survivor clasts from large to small survivor clasts. A brighter portion of the image indicates a higher density; darker indicates less dense. A) HGCR4S3 UTCT scans B) HGCR4S4 UTCT scans.

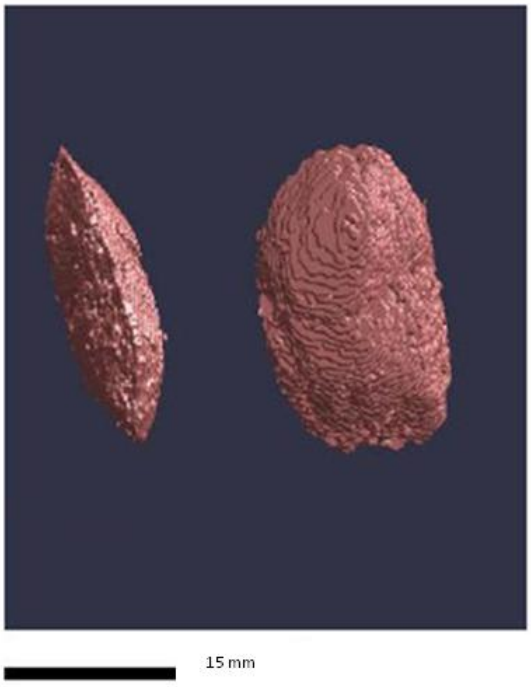

Figure 14. UTCT scan data rendering of a “Blob”. Note the fine well defined boundaries of the rendered survivor clast.

a.

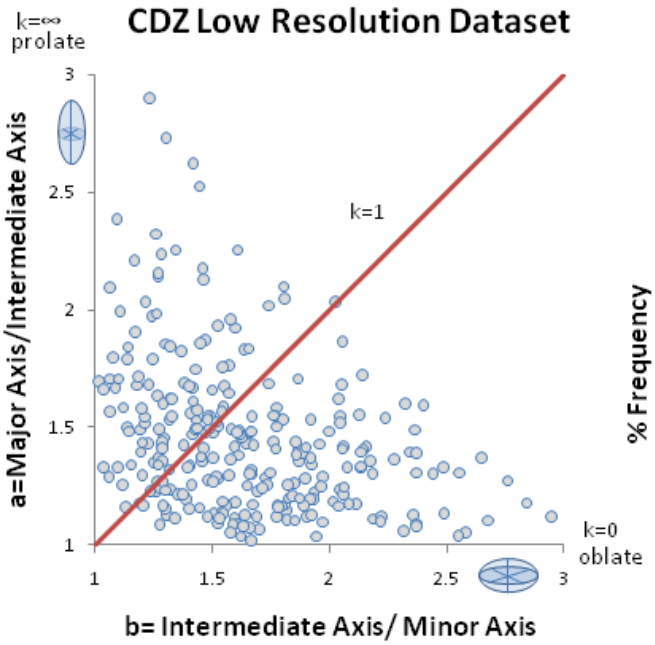
CDZ Low Resolution Dataset
k=∞
prolate
a=Major Axis/Intermediate Axis
k=1
k=0
oblate
b= Intermediate Axis/ Minor Axis
1
1.5
2
2.5
3

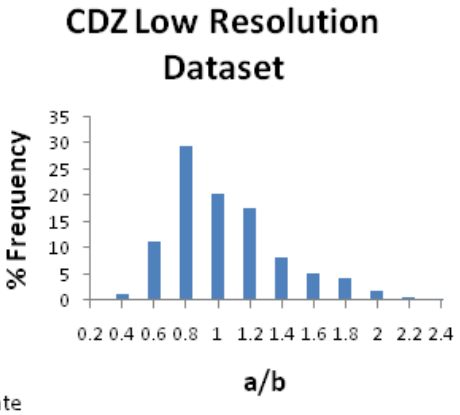
CDZ Low Resolution Dataset
% Frequency
a/b
0 5 10 15 20 25 30 35
0.2 0.4 0.6 0.8 1 1.2 1.4 1.6 1.8 2 2.2 2.4

b.

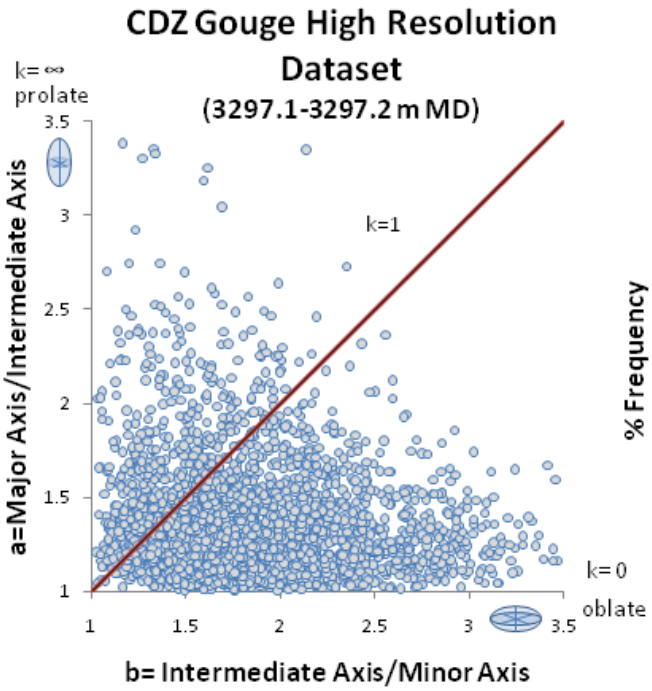
CDZ Gouge High Resolution Dataset
(3297.1-3297.2 m MD)
k= ∞
prolate
a=Major Axis/Intermediate Axis
k=1
k= 0
oblate
b= Intermediate Axis/Minor Axis
1
1.5
2
2.5
3
3.5

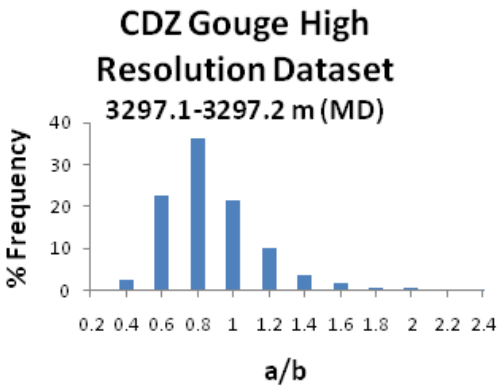
CDZ Gouge High Resolution Dataset
3297.1-3297.2 m (MD)
% Frequency
a/b
0 10 20 30 40
0.2 0.4 0.6 0.8 1 1.2 1.4 1.6 1.8 2 2.2 2.4

c.

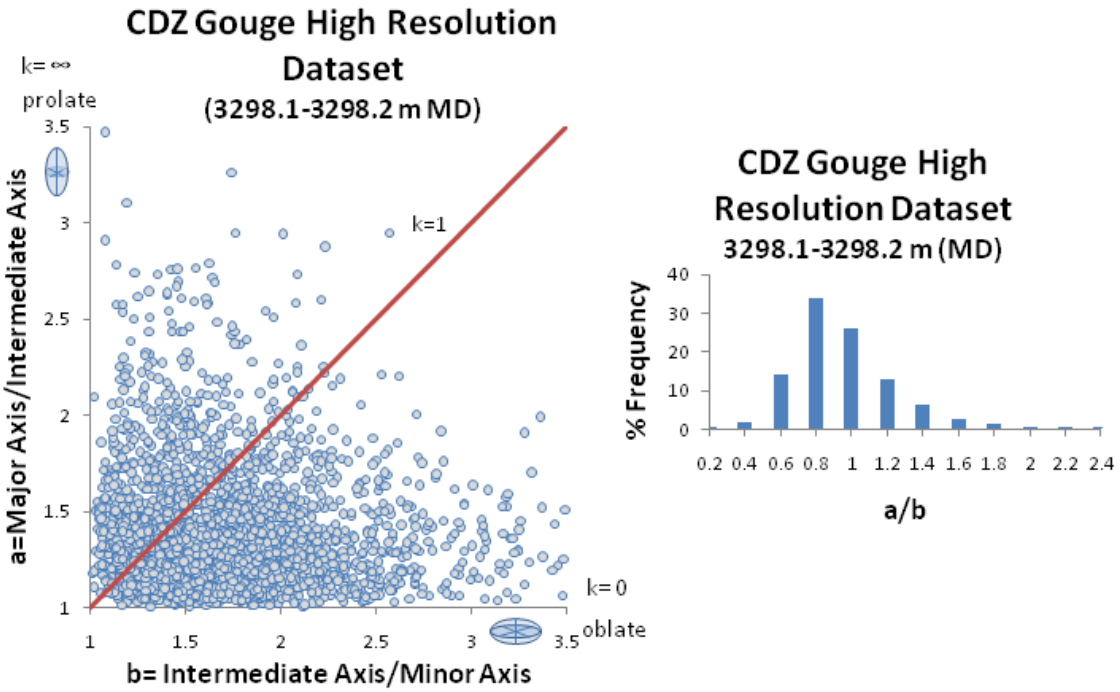

Figure 15. Flinn diagrams of ellipsoidal shaped survivor clasts from the CDZ gouge zone. In the diagram, K = ∞ (Y axis) describes prolate uniaxial ellipsoids, values from 1< k < ∞ describe prolate triaxial ellipsoids, k = 1 describes scalene ellipsoids, 0 < k <1 describes oblate triaxial ellipsoids, and k = 0 (X axis) describes all oblate uniaxial ellipsoids [*Flinn*, 1962]. The percent frequency histograms represent the statistical shape distribution in the Flinn diagrams. (a.) CDZ gouge low resolution dataset. (b) High Resolution Images 3297.1-3297.2 m (MD) Flinn diagram with statistical histogram. (c) High Resolution Images 3298.1-3298.2 m (MD) Flinn diagram with statistical histogram.

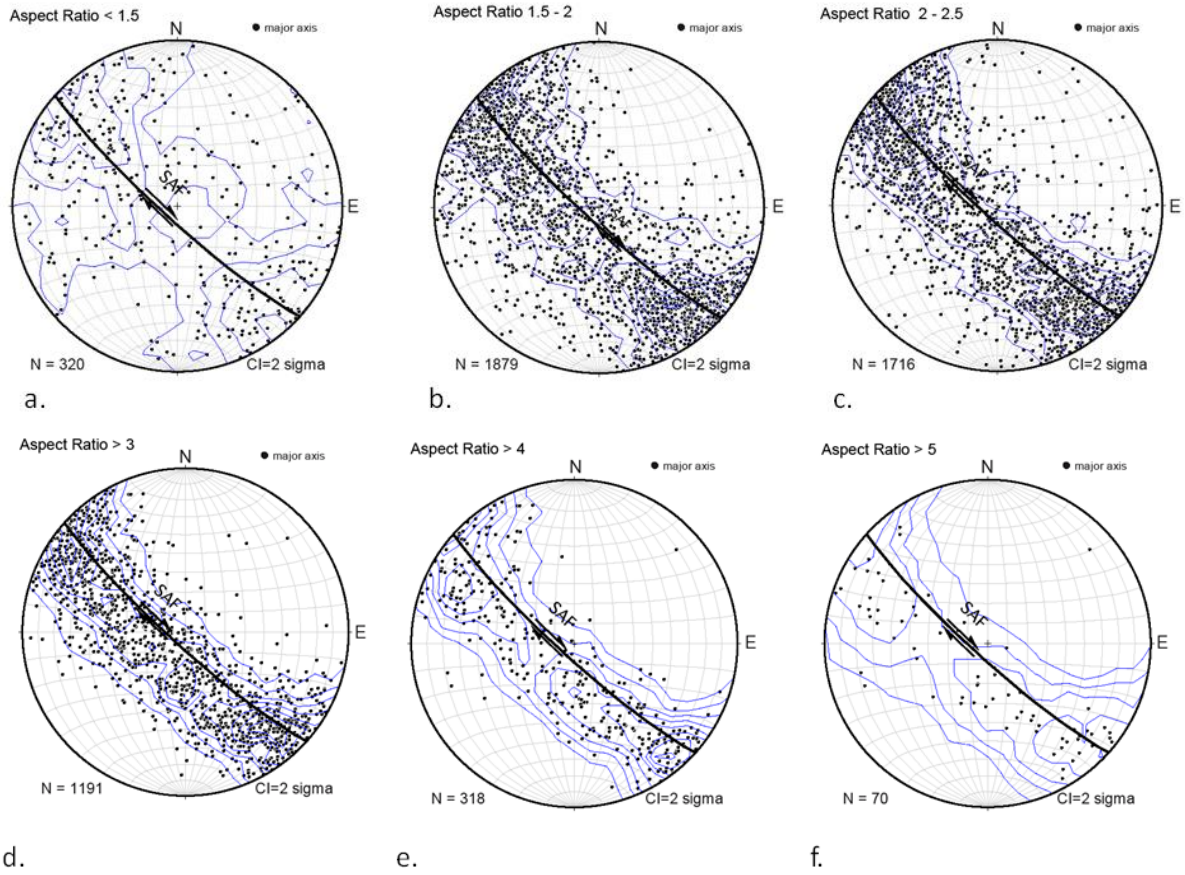

Figure 16. Orientation distribution of survivor clasts from the CDZ gouge as a function of aspect ratio location. Lower Hemisphere Equal Area Projections of Survivor Clasts major axes rotated into geographic orientation assuming pure strike-slip kinematics and orientation distribution data from the SDZ gouge clasts. Major axis is indicated by solid black circles. Contoured using Kamb method with three sigma contour interval. (a.) aspect ratio <1.5 (b.) aspect ratio 1.5-2 (c.) aspect ratio 2-2.5 (d.) aspect ratio > 3(e.) aspect ratio > 4 (f.) aspect ratio > 5.

a.

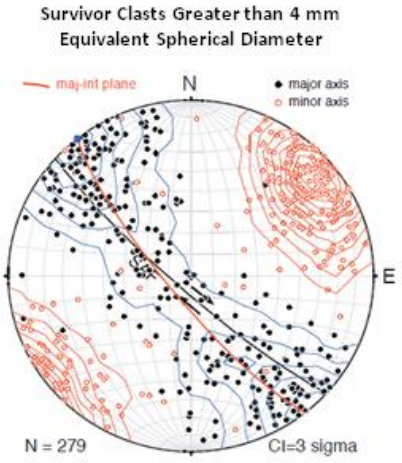
Survivor Clasts Greater than 4 mm
Equivalent Spherical Diameter
maj-int plane
major axis
minor axis
N
E
N = 279
CI=3 sigma

b.

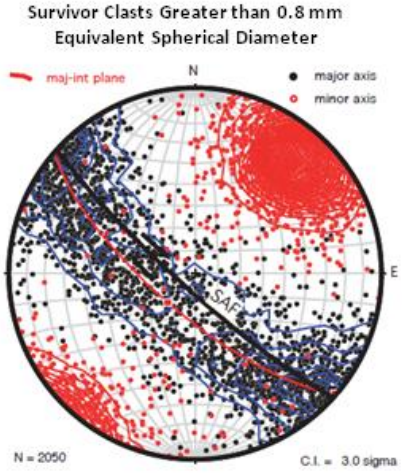
Survivor Clasts Greater than 0.8 mm
Equivalent Spherical Diameter
maj-int plane
major axis
minor axis
N
E
SAF
N = 2050
C.I. = 3.0 sigma

c.

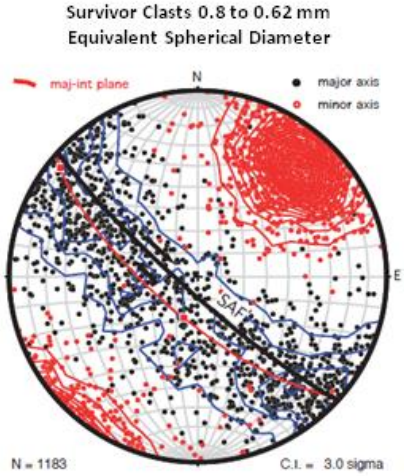
Survivor Clasts 0.8 to 0.62 mm
Equivalent Spherical Diameter
maj-int plane
major axis
minor axis
N
E
SAF
N = 1183
C.I. = 3.0 sigma

d.

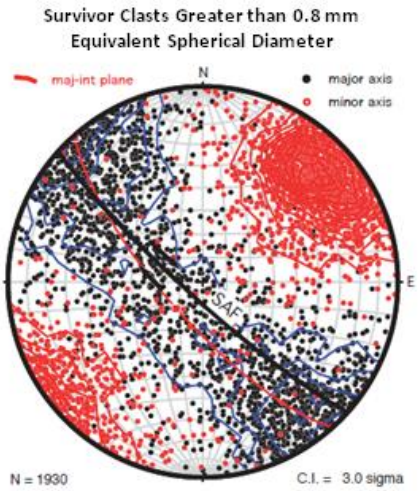
Survivor Clasts Greater than 0.8 mm
Equivalent Spherical Diameter
maj-int plane
major axis
minor axis
N
E
SAF
N = 1930
C.I. = 3.0 sigma

e.

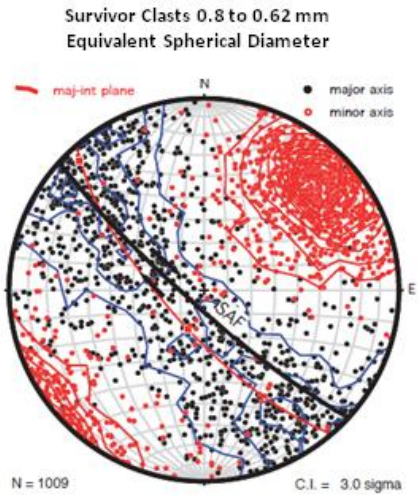
Survivor Clasts 0.8 to 0.62 mm
Equivalent Spherical Diameter
maj-int plane
major axis
minor axis
N
E
SAF
N = 1009
C.I. = 3.0 sigma

Figure 17. Orientation distribution of survivor clasts from the CDZ gouge as a function of size and location. The orientation distributions are plotted in lower hemisphere equal area projections. The poles of the major and minor axes of survivor clasts are rotated into geographic orientation assuming pure strike-slip kinematics. Major axis is indicated by solid black circles and minor axis is indicated by open red circles. The foliation is denoted by the bingham major axes and corresponding plane in red. Contoured using Kamb method with three sigma contour interval. (a.) CDZ low resolution images and corresponding clasts. (b.) CDZ high resolution images of 3297.1-3297.2 m (MD) survivor clasts greater than 0.8 mm equivalent spherical diameter (c.) CDZ high resolution scans of 3297.1-3297.2 m (MD) survivor clasts with equivalent spherical diameter between 0.8 and 0.62 mm. (d.) CDZ high resolution scans of 3298.1-3298.2 m (MD) survivor clasts greater than 0.8 mm equivalent spherical diameter. (e.) CDZ high resolution scans of 3298.1-3298.2 m (MD) survivor clasts between 0.8 and 0.62 mm equivalent spherical diameter

a.

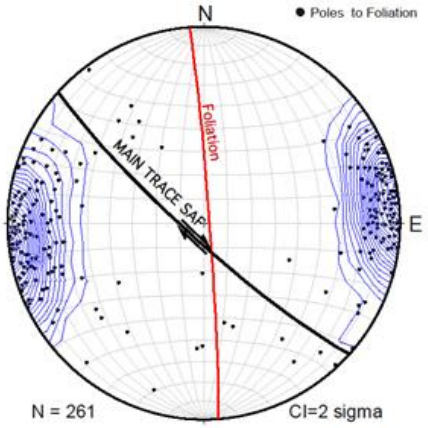

b.

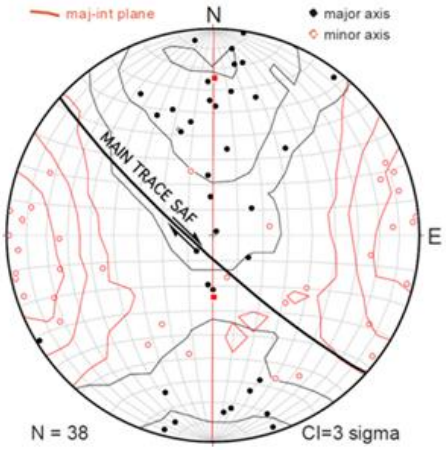

Figure 18. Foliation fabric and orientation distribution of survivor clasts from the foliated cataclasites west of the SDZ. Contoured using Kamb method with three sigma contour interval. Orientation from drilling survey data and borehole rotation from image log data. (a.) Foliation fabric from the foliated cataclasites west of the SDZ over the 3186.7-3190.7 m (MD) interval. The poles and contours show normals to all foliation planes. Great circle shows the best fit foliation defined by the fisher distribution of normals to all foliation planes (353, 87 E) (b.) Foliation fabric from the foliated cataclasites west of the SDZ over the 3191-3194 m (MD) interval. The poles and contours show normals to all foliation planes. Great circle shows the best fit foliation defined by the fisher distribution of normals to all foliation planes (357, 88 E) (c.) Survivor clasts from the foliated cataclasites west of the SDZ. Major axis is indicated by solid black circles and minor axis is indicated by open red circles. The foliation is denoted by the bingham major axes and corresponding plane in red.

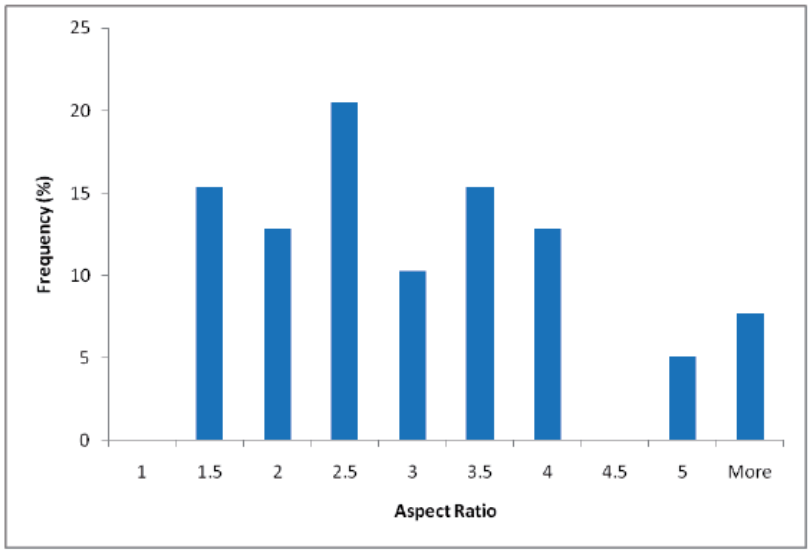

a.

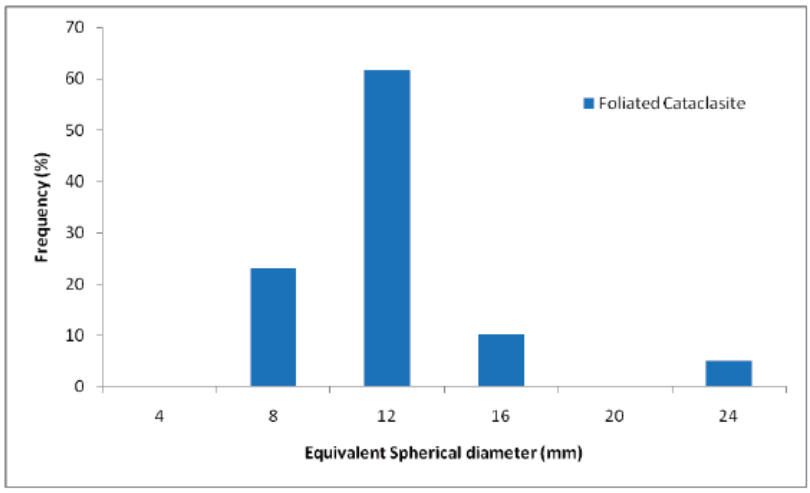

b.

Figure 19. Histogram of axial ratios and histogram of equivalent spherical diameters (mm) for the survivor clasts from the foliated cataclasites west of the SDZ. (a.) Axial ratio (b.) Equivalent spherical diameter (mm).

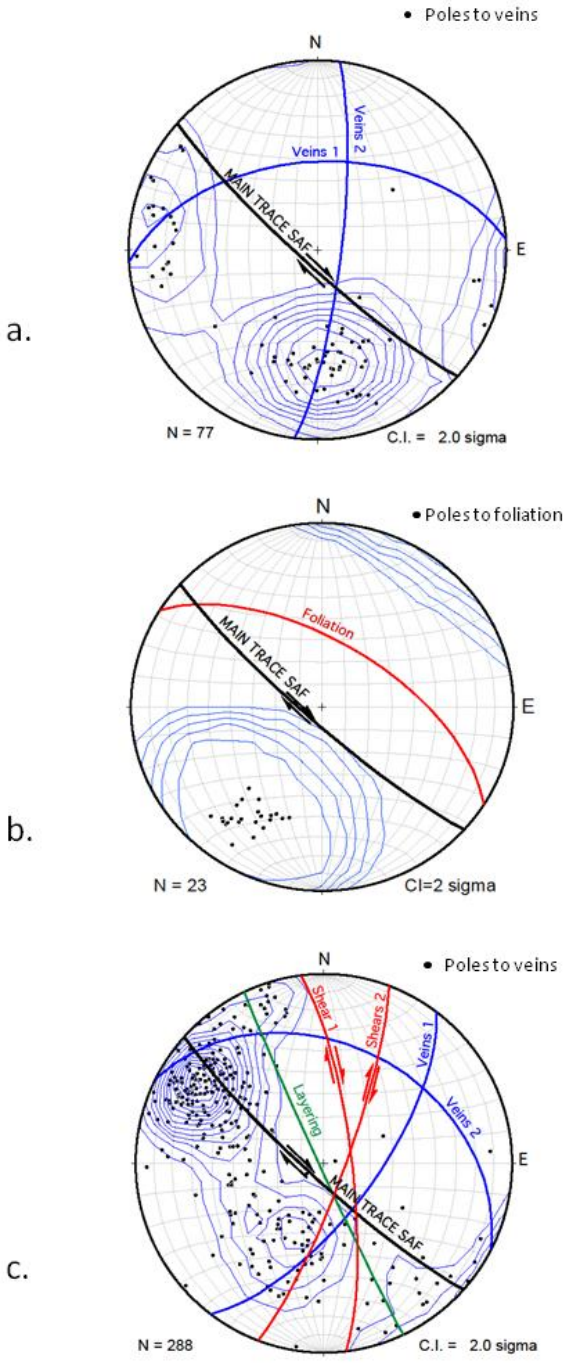

Figure 20. Fabric of veins, foliations, shears and layering of fault rock adjacent to the west and east SDZ foliated fault gouge. Contoured using Kamb method with two sigma contour interval (a.) Orientation distribution of veins within the massive shale west of the SDZ. The poles and contours show normals to veins. Great circle shows the best fit

veins for the dominant and minor veins sets defined by the fisher distribution of normals to all veins. The dominant vein set has a 6.8, 79.7 E orientation and the minor vein set has a 266.6, 51.4 N orientation. (b.) Fabric of foliations from the foliated cataclasites adjacent to the SDZ gouge. The poles and contours show normals to foliations. Great circle shows the best fit foliation by the fisher distribution of normals to all foliations (302, 61 N). (c.) Orientation distribution of veins, shears, and layering from the interbedded sandstones and siltstones, from the northeast side of the southwest creeping zone. The poles and contours show normals to veins. Great circles show the orientation of shears (353, 78 E and 20, 81 E), shale layering (334, 88 SW), and the best fit veins for the dominant and minor veins sets defined by the fisher distribution of normals to all veins. The dominant vein set has a 37, 68 E orientation and the minor vein set has a 297, 37, N orientation.

VITA

Name:	David Wayne Sills
Address:	EOG Resources, Inc., North Division 421 West 3rd Street, Suite 150 Fort Worth, Texas 76102
Email Address:	David_Sills@eogresources.com
Education:	B.S., Geology, Sam Houston State University, 2006 M.S., Geology, Texas A&M University, 2010
Professional Experience:	EOG Resources, Geologist 1 July 2010 EOG Resources, Intern, Summer 2009 Core Laboratories, Intern, Summer 2008
Teaching:	Texas A&M, 2007-2010 Sam Houston State University, 2004-2007

`